Geothermal Energy

RESEARCH Open Access

Optimized geothermal energy extraction from hot dry rocks using a horizontal well with different exploitation schemes

Guoshu Huang[1,2], Xiangyun Hu[1*], Huolin Ma[1], Liang Liu[2], Jian Yang[1], Wenlong Zhou[1], Weiyang Liao[1] and Bai Ningbo[1]

*Correspondence:
xyhu@cug.edu.cn

[1] Hubei Subsurface Multi-Scale Imaging Key Lab, Institute of Geophysics and Geomatics, China University of Geosciences-Wuhan, 430074 Wuhan, People's Republic of China
[2] Present Address: Department of Earth Science and Engineering, Shanxi Institute of Technology, Yangquan 045000, China

Abstract

In the foreseeable future, the geothermal exploitation from hot dry rocks (HDR) using a horizontal well will bear potential. Thus, in-depth studies should be conducted on the selection of injection-production scheme (IPS) and working fluid, design of reinjection parameters, optimization of wellbore structure and materials, and analysis of geological settings. This paper proposed a fully coupled model to study the above scientific questions. For Model A, the working fluid was injected into the annulus and then flowed out of the thermal insulation pipe (TIP). Its temperature passes through two stages of temperature rise and two stages of temperature decline. But for model B, the working fluid was injected into the TIP and then flowed out of the annulus. Its temperature undergoes five stages, four stages of temperature rise and one stage of temperature decline. The results show that the Model A is the best IPS owing to its high outlet temperature, stable thermal recovery, and low fluid injection volume. In Model A, when the working fluid was supercritical carbon dioxide and the liquid injection volume was 135.73 m^3/d, the heat recovery ratio (HRR) was as high as 85.40%, which was 17.85% higher than that of the Model B whose working medium was water, and its liquid injection volume was only 25% of that. Meanwhile, over ten years of continuous production, the outlet temperature decreased by 7.5 °C and 18.38 °C in the latter. The optimal working fluid has a low volume heat capacity and thermal conductivity for any IPS. Sensitivity studies showed that for the area that met the HDR standard, the effect of reinjection temperature on the outlet temperature can be ignored. As for Model A, HRR drops sharply by 6.74–9.32% when TIP goes from completely adiabatic to nonzero thermal conductivity. Meanwhile, the horizontal segment length of the TIP is shorter when Model A obtains the optimal outlet temperature compared with Model B. In addition, the correlation between the outlet temperature and different formations of thermophysical properties was seriously affected by the IPS and exploitation period, which was summarized in detail.

Keywords: Horizontal well, Geothermal exploitation, Hot dry rocks, Working fluids, Injection-production modes, Optimization scheme

Introduction

Geothermal energy is one of the promising supplements to fossil fuels (Sayigh 1999; Gupta and Roy 2006); it is characterized as reproducible and nonpolluting (Esen et al. 2007a, 2007b; Balbay and Esen 2013; Gharibi et al. 2018; Nian and Cheng 2018). In addition, geothermal resources are almost inexhaustible and barely affected by weather conditions (Adams et al. 2014; Aliyu and Chen 2017; Arat and Arslan 2017; Liu et al. 2018), different from weather-dependent energy sources (tidal, wind, and solar energies). Thus, geothermal resources, especially for hot dry rocks (HDR), have received considerable research attention because of their huge potential for electricity generation and space heating (Lee 2014; Li and Zhang 2017; Willems et al. 2017; Zeng et al. 2017; Shi et al. 2018, 2019). Since the Fenton Hill project in the 1970s (Lu 2018), enhanced geothermal system (EGS) technology has developed over the past 50 years in several countries. Although EGS was not first applied in the EU, France's Soultz plant and Germany's Landau plant were the first two commercial-scale EGS power plants. EGS development has also been ambitious in Australia. The world's largest EGS power plant was schedule to be operational in Habanero, Australia, a 1 MWe demonstration EGS power plant began operating at the beginning of May 2013 (Asai et al. 2018; Lu 2018; Gong et al. 2020).

Given HDR's extremely low porosity and permeability, large-scale hydro-fracturing is usually required before geothermal exploitations to provide channels for flow and heat exchange (None 2009; Wang et al. 2012a, 2012b; Li et al. 2022). However, the fractures created by hydro-fracturing can be blocked under geo-stress and water–rock interactions, rendering geothermal resources unexploitable (Xu and Pruess 2004; Pruess 2006). On the other hand, cap rocks can be easily fractured because of their high brittleness, which results in a huge loss of water (Hendron 1987; Brown et al. 1999; Brown and Duchane 1999). Large-scale hydro-fracturing is not only expensive but can also cause environmental problems or induce earthquakes (Majer et al. 2007; Kraft and Deichmann 2014; Anyim and Gan 2020). Therefore, an economical, environmentally friendly, safe, and reliable method must be developed for the enhanced geothermal exploitation of HDR.

One commonly adopted method for geothermal exploitation of HDR is circulating the working fluids through wellbores (Brown 2000; Pruess 2006; Zhang et al. 2013; Wang et al. 2018), in which the costly and complex hydro-fracturing can be avoided. In addition, oil and gas wells have been increasingly abandoned worldwide when petroleum reservoirs became depleted without economic feasibility. Therefore, numerous researchers began to study abandoned oil and gas wells (AOGW) for heat extraction and power generation. If the AOGW can be retrofitted to geothermal systems for the extraction of thermal energy from the HDR, not only can the environmental risk be reduced effectively, but the geothermal utilizations will also become cheaper without high-cost drilling (Su and Sun 1996; Wang and Liu 1997; Nian and Cheng 2018).

Kujawa et al. (2004, 2005) proposed the seminal research of retrofitting AOGW for geothermal production based on a double-pipe heat exchanger and assessed the possibility and usefulness of accessing geothermal energy from existing production wells (Kujawa et al. 1998, 2003). Subsequently, significant advances (Davis and Michaelides 2009; Bu et al. 2012; Cheng et al. 2013; Angrisani et al. 2016; Mokhtari et al. 2016) have occurred in the AOGW for geothermal energy production, but previous models

were focused on vertical wells, which cannot be used for simulating the unique heat and mass transfer characteristics of the flow in a horizontal well. Many works have been done on a horizontal ground-coupled heat pump systems in shallow strata (Esen et al. 2007a, 2007b; Gonzalez et al. 2012; Go et al. 2016; Bulmez et al. 2022). However, there is little research on heat extraction from horizontal wells in deep strata. Thus, Cui et al. (2017) and Sun et al. (2018) attempted to study the performance of geothermal development in horizontal wells, and the technical and economic feasibility was also assessed. In addition, based on the updated conceptual model of the field, Seyedrahimi-Niaraq et al. (2021a, 2021b) presented an unsaturated numerical model for the NW Sabalan geothermal reservoir by incorporating some new exploration data and considering the unsaturated zone. For predicting the reservoir production capacity, a 30-year production response for the various electricity generation scenarios was carried out and the optimal production zone was determined.

However, no scholars have dynamically analyzed the heat extraction of a horizontal well with different exploitation schemes from the time–space perspective. In addition, we believe that in the foreseeable future, geothermal development using a horizontal well will be a potential heat recovery method. For this purpose, in-depth studies should focus on selecting injection-production scheme (IPS) and working fluids, design of reinjection parameters, optimization of wellbore structure and materials, and analysis of thermophysical geological properties.

A fully coupled model was proposed to study the geothermal exploitation of HDR by recycling water/supercritical carbon dioxide (SCCO) in a horizontal well via a closed loop. In addition, two kinds of IPS were focused on in this study: (a) Fluid is injected into the annulus and then flows out of the thermal insulation pipe (TIP). (b) Fluid is injected into the TIP and then flows out of the annulus. To better describe the heat exchange in geothermal exploitations under transient temperature and pressure, the thermophysical parameters of the working fluids were obtained by dynamically invoking the database of the National Institute of Standards and Technology (NIST). In addition, to study the different IPS, we put forward the "injection-production switch" parameters. We first investigated each exploitation mode's optimal reinjection rate (q_{best}) based on the outlet temperature. In addition, we studied the mode with the highest outlet temperature and that with the most stable thermal recovery. Then, we dynamically analyzed the effects of various factors on the geothermal exploitation performance under different IPS, working fluids, and exploitation periods (t_{exp}). The factors were divided into three main categories: (a) reinjection parameters, (b) wellbore structure and materials, and (c) geological factors. Finally, for the four exploitation modes, the variation coefficients of the outlet temperatures corresponding to various sensitivity parameters were calculated, which can contribute to the integrated optimization of geothermal extraction schemes.

The superiority of this model over the previous models presents a comprehensive and more realistic numerical model for the geothermal exploitation of a horizontal well and predicts the performance of the different production scenarios. There are mainly three contributions of this paper to the previous research: (a) Type curve analyses were used to understand complex heat exchanging processes for different exploitation modes. (b) Key design variables were deeply discussed from the space–time perspective to obtain

conceptual design guidelines. (c) The correlation between the outlet temperature and different stratum of thermophysical properties was summarized in detail.

Modeling

Figure 1 depicts the structure of the horizontal well for geothermal exploitation. The bottom of the wellbore, which is different from the wells used in oilfields, was sealed with cement or packer to prevent direct contact between the injected working fluids and the rock (Cui et al. 2017). In addition, two kinds of IPS (fluid loop) were used to extract heat:

a) [Model A] (Fig. 1a): The fluid is injected into the annulus and then flows out of the TIP. The injected low-temperature working fluid flows through the annulus between the TIP and casing along the wellbore, being heated up simultaneously by the geothermal reservoir. At the bottom of the horizontal well, the heated fluid with the highest temperature flows into the TIP and returns to the surface for heat exchange.
b) [Model B] (Fig. 1b): The fluid is injected into the TIP and then flows out of the annulus. The heat-transmission fluid is first injected into the TIP of the vertical segment, followed by the working fluid to the well bottom, after which flow begins and proceeds toward the horizontal segment of the TIP. When the working fluid reaches the toe point of the long horizontal tube, it begins to flow into the annulus where it extracts heat energy from the surrounding HDR.

In addition, the heated working fluids were pumped to the ground through the vertical wellbore for residential heating or electricity generation: at present, the most common technology in geothermal power generation is the dual cycle geothermal power system, including the organic Rankine cycle and the Kalina cycle (Wu et al. 2009; Bina et al. 2018). The main principle of the system is that the high-temperature geothermal fluid is pumped into a heat exchanger to transfer its thermal energy to another working medium (usually a low-boiling working fluid), which is heated and evaporated into a steam turbine to do work to generate electricity. After completion of the heat exchange (generate electricity), the cooled working fluid was used for reinjection.

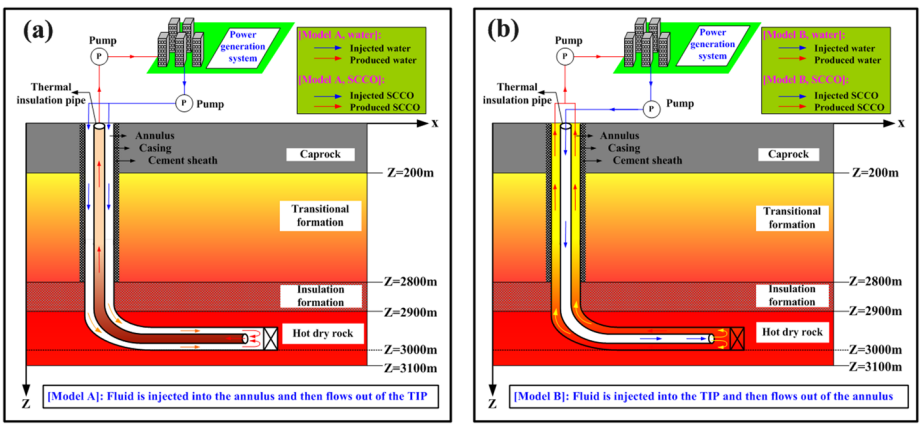

Fig. 1 Schematic of different IPS for geothermal exploitation of a horizontal well

To facilitate the research, we defined four exploitation modes in which the working fluid can be water or SCCO:

(1) [Model A, water] representing the IPS of [Model A] and with water as the working fluid;
(2) [Model A, SCCO] representing the IPS of [Model A] and with SSCO as the working fluid;
(3) [Model B, water] representing the IPS of [Model B] and with water as the working fluid;
(4) [Model B, SCCO] representing the IPS of [Model B] and with SCCO as the working fluid.

In addition, to facilitate the description of the relevant thermal extraction process, we abbreviated the pipes of different segments as follows (the same below):

(1) TIP_V represents the vertical segment of the TIP.
(2) TIP_H represents the horizontal segment of the TIP.
(3) ANN_H represents the horizontal segment of the annulus.
(4) ANN_V represents the vertical segment of the annulus.

Transient temperature field governing equation of the model

In accordance with the heat flow process of the model, the temperature field governing equation can be derived. The implicit difference method was used to solve the transient temperature distribution in this research. In addition, Appendix A shows the mesh generation method of the thermal extraction system.

Heat transfer model inside the vertical pipes

Conduction and convection dominated the heat transfers of the working fluids in the vertical pipes (including the TIP_V and ANN_V) during the exploitation. In addition, in the vertical pipes of the wellbore, the vertical component of the working fluid's downward/upward seepage velocity was highly valued, and the radial component can be neglected (Huang et al. 2019; Xu 2020; Zhang et al. 2021). Thus, the heat transfer equation inside the vertical pipes can be written as follows:

$$\frac{\partial}{\partial x}\left(\lambda_f \frac{\partial T}{\partial x}\right) + \frac{\partial}{\partial z}\left(\lambda_f \frac{\partial T}{\partial z}\right) - \frac{\partial}{\partial z}\left(\rho_f c_f v_z T\right) = \frac{\partial}{\partial t}\left(\rho_f c_f T\right) \tag{1}$$

where T is the temperature field, v_z is the seepage velocity of the working fluid in the vertical pipes, and λ_f, ρ_f and c_f represent the thermal conductivity, density and specific heat capacity of the working fluid, respectively.

In the vertical wellbore, the flow direction of the working fluid in the annulus was opposite that of the working fluid in the TIP. Therefore, for this research, we innovatively put forward the "injection-production switch" parameters (S_1, S_2, and S_3), which can be used to define the convection terms of the governing equation with different flow directions of the working fluid:

$$\begin{cases} S_1 = \frac{v_z+|v_z|}{2|v_z|} \\ S_2 = \frac{v_z}{|v_z|} \\ S_3 = \frac{v_z-|v_z|}{2|v_z|} \end{cases} \tag{2}$$

In the vertical conduit, when the flow direction of the working fluid is downward, $v_z > 0$; otherwise, $v_z < 0$. Thus, S_1, S_2, and S_3 were all constants. In addition, if $v_z > 0$, then $S_1 = 1$, $S_2 = 1$, $S_3 = 0$; if $v_z < 0$, $S_1 = 0$, $S_2 = -1$, and $S_3 = -1$. In addition, the upwind difference scheme was adopted for the convection term (Ewing et al. 1994; Lazarov et al. 1996; Yuan 2010; Shi 2021):

$$\frac{\partial}{\partial z}\left(\rho_f c_f v_z T\right) = \frac{\rho_f c_f v_z}{\Delta z}\left(-s_1 T_{i,j-1}^{n+1} + s_2 T_{i,j}^{n+1} - s_3 T_{i,j+1}^{n+1}\right) \tag{3}$$

where $T_{i,j-1}^{n+1}$, $T_{i,j}^{n+1}$ and $T_{i,j+1}^{n+1}$ represent the temperature at the next time period in discrete grid nodes $(i, j-1)$, (i, j) and $(i, j+1)$, respectively.

The difference scheme of Eq. (1) can be defined as follows:

$$\begin{aligned} &a_1\left(T_{i+1,j}^{n+1} - 2T_{i,j}^{n+1} + T_{i-1,j}^{n+1}\right) + a_2\left(T_{i,j+1}^{n+1} - 2T_{i,j}^{n+1} + T_{i,j-1}^{n+1}\right) \\ &- a_3\left(-s_1 T_{i,j-1}^{n+1} + s_2 T_{i,j}^{n+1} - s_3 T_{i,j+1}^{n+1}\right) = a_4\left(T_{i,j}^{n+1} - T_{i,j}^{n}\right) \end{aligned} \tag{4}$$

where $T_{i,j}^{n}$ is the current temperature in the discrete grid nodes (i, j), and $T_{i+1,j}^{n+1}$ and $T_{i-1,j}^{n+1}$ represent the temperature at the next time period in discrete grid nodes $(i+1, j)$ and $(i-1, j)$, respectively.

Equation (4) can be simplified as below:

$$\begin{aligned} &a_1 T_{i-1,j}^{n+1} + (-2a_1 - 2a_2 - s_2 a_3 - a_4) T_{i,j}^{n+1} + a_1 T_{i+1,j}^{n+1} \\ &+ (a_2 + s_1 a_3) T_{i,j-1}^{n+1} + (a_2 + s_3 a_3) T_{i,j+1}^{n+1} = -a_4 T_{i,j}^{n} \end{aligned} \tag{5}$$

where

$$a_1 = \frac{(\lambda_f)^{t-1}}{(\Delta x)^2}, a_2 = \frac{(\lambda_f)^{t-1}}{(\Delta z)^2}, a_3 = \frac{\left(\rho_f c_f\right)^{t-1} v_z}{\Delta z}, a_4 = \frac{\left(\rho_f c_f\right)^{t-1}}{\Delta t} \tag{6}$$

where Δt is the time step, and Δx and Δz are the radial and discrete longitudinal spacing, respectively.

Heat transfer model inside the horizontal pipes

Heat conduction and convection dominated the heat transfer of the working fluids in the horizontal conduits (including the TIP_H and ANN_H). Thus, the temperature field equation can be expressed as follows (Huang et al. 2019; Wang 2019; Zhang et al. 2021):

$$\frac{\partial}{\partial x}\left(\lambda_f \frac{\partial T}{\partial x}\right) + \frac{\partial}{\partial z}\left(\lambda_f \frac{\partial T}{\partial z}\right) - \frac{\partial}{\partial x}\left(\rho_f c_f v_r T\right) = \frac{\partial}{\partial t}\left(\rho_f c_f T\right) \tag{7}$$

where T is the temperature field, v_r is the seepage velocity of the working fluid in the horizontal pipes, and λ_f, ρ_f and c_f represent the thermal conductivity, density and specific heat capacity of the working fluid, respectively. In the same manner, the upwind difference scheme was adopted for the convection term (Ewing et al. 1994; Lazarov et al. 1996; Yuan 2010; Shi 2021):

$$\frac{\partial}{\partial x}\left(\rho_f c_f v_r T\right) = \frac{\rho_f c_f v_r}{\Delta x}\left(-s_1 T_{i-1,j}^{n+1} + s_2 T_{i,j}^{n+1} - s_3 T_{i+1,j}^{n+1}\right) \tag{8}$$

where $T_{i-1,j}^{n+1}$, $T_{i,j}^{n+1}$ and $T_{i+1,j}^{n+1}$ represent the temperature at the next time period in discrete grid nodes $(i-1, j)$, (i, j) and $(i+1, j)$, respectively.

The difference scheme of Eq. (7) can be defined as follows:

$$c_1 T_{i-1,j}^{n+1} + (-2c_1 - 2c_2 - s_2 c_3 - c_4) T_{i,j}^{n+1} + c_1 T_{i+1,j}^{n+1} + (c_2 + s_1 c_3) T_{i,j-1}^{n+1} + (c_2 + s_3 c_3) T_{i,j+1}^{n+1} = -c_4 T_{i,j}^{n} \tag{9}$$

where

$$c_1 = \frac{(\lambda_f)^{t-1}}{(\Delta x)^2}, c_2 = \frac{(\lambda_f)^{t-1}}{(\Delta z)^2}, c_3 = \frac{\left(\rho_f c_f\right)^{t-1} v_r}{\Delta x}, a_4 = \frac{\left(\rho_f c_f\right)^{t-1}}{\Delta t} \tag{10}$$

where Δt is the time step, Δx is the discrete radial spacing, Δz is the discrete longitudinal spacing, $T_{i,j}^{n}$ is the current temperature in the discrete grid nodes (i, j), and $T_{i+1,j}^{n+1}$ and $T_{i-1,j}^{n+1}$ represent the temperature at the next time period in discrete grid nodes $(i+1, j)$ and $(i-1, j)$, respectively.

Heat transfer model for the HDR and impermeable medium

For the HDR and impermeable medium (pipes/cements), heat conduction dominates the heat transfer rather than convection. Thus, their transient temperature field governing equation can be given by the following (Fang 2018; Huang et al. 2019):

$$\frac{\partial}{\partial x}\left(\lambda_s \frac{\partial T}{\partial x}\right) + \frac{\partial}{\partial z}\left(\lambda_s \frac{\partial T}{\partial z}\right) = \frac{\partial}{\partial t}(\rho_s c_s T) \tag{11}$$

where T is the temperature field, and λ_s, ρ_s and c_s represent the thermal conductivity, density and specific heat capacity of the impermeable media, respectively.

The difference scheme of Eq. (11) can be defined as follows:

$$b_1 T_{i-1,j}^{n+1} + (-2b_1 - 2b_2 - b_3) T_{i,j}^{n+1} + b_1 T_{i+1,j}^{n+1} + b_2 T_{i,j-1}^{n+1} + b_2 T_{i,j+1}^{n+1} = -b_3 T_{i,j}^{n} \tag{12}$$

where

$$b_1 = \frac{(\lambda_s)^{t-1}}{(\Delta x)^2}, b_2 = \frac{(\lambda_s)^{t-1}}{(\Delta z)^2}, b_3 = \frac{(\rho_s c_s)^{t-1}}{\Delta t} \tag{13}$$

where Δt is the time step, Δx is the discrete radial spacing, Δz is the discrete longitudinal spacing, $T_{i,j}^{n}$ is the current temperature in the discrete grid nodes (i, j), and $T_{i-1,j}^{n+1}$, $T_{i,j}^{n+1}$,

$T_{i+1,j}^{n+1}$ $T_{i,j-1}^{n+1}$ and $T_{i,j+1}^{n+1}$ represent the temperature at the next time period in discrete grid nodes $(i-1, j)$, (i, j), $(i+1, j)$, $(i, j-1)$ and $(i, j+1)$, respectively.

Initial and boundary conditions of the model

The initial (undisturbed) geothermal temperature was assumed to be a known function of depth. Thus, the initial condition can be written as follows:

$$T|_{t=0} = T_{\text{sur}} + g_T z \tag{14}$$

where T_{sur} is the initial surface temperature, and g_t is the geothermal gradient.

The inner/outer boundary of the temperature field was assumed to be equal to the (undisturbed) geothermal temperature. Therefore, the model's inner and outer boundary conditions can be defined by Eqs. (15) and (16), respectively. In the vertical pipes, the coupled boundary conditions at the interfaces between the working fluids and tube walls can be given by Eq. (17). In addition, the coupled boundary conditions at the interfaces between the working fluids in the vertical and horizontal pipes can be described as Eq. (18).

$$T|_{r=0} = T_{\text{sur}} + g_T z \tag{15}$$

$$T|_{r=r_e} = T_{\text{sur}} + g_T z \tag{16}$$

$$\begin{cases} h_c\left(T_{\text{bf}} - T_{\text{bp}}\right) = -\lambda_s \frac{\partial T}{\partial r}|_{r=r_{\text{fp}}} \\ T_{\text{bf}}|_{r=r_{\text{fp}}} = T_{\text{bp}}|_{r=r_{\text{fp}}} \end{cases} \tag{17}$$

$$\begin{cases} \lambda_f \frac{\partial T}{\partial r}|_{r=r_{\text{vh}}} + |\rho_{\text{f}} c_{\text{f}} v_r|(T_{\text{vf}} - T_{\text{hf}})|_{r=r_{\text{vh}}} = \lambda_s \frac{\partial T}{\partial r}|_{r=r_{\text{vh}}} \\ T_{\text{vf}}|_{r=r_{\text{vh}}} = T_{\text{hf}}|_{r=r_{\text{vh}}} \end{cases} \tag{18}$$

$$h_{\text{c}} = 0.023 \frac{\lambda_{\text{f}}}{L} R_{\text{ef}}^{0.8} P_{\text{rf}}^{n} \tag{19}$$

where r_e is the radial distance from the left boundary to the right, r_{fp} is the boundary between the working fluid and the vertical pipe, r_{vh} is the boundary between the working fluids in the vertical pipe and working fluids in the horizontal pipe, T_{bf} and T_{bp} are the working fluid temperature and vertical pipe temperature at the working fluid/vertical, T_{vf} and T_{hf} are the working fluid temperature in the vertical pipe and the working fluid temperature in the horizontal pipe at the horizontal pipe/vertical pipe interface, λ_{s} represents the thermal conductivity of the impermeable media, and λ_{f}, ρ_{f} and c_{f} represent the thermal conductivity, density and specific heat capacity of the working fluid, respectively. In addition, h_{c} is the convection heat transfer coefficient, L is the characteristic length, R_{ef} is Reynolds number, P_{rf} is Prandtl number, n is the coefficient, and $n = 0.3$ (when the fluid is heated) or $n = 0.2$ (when the fluid is cooled).

In the longitudinal direction, we assumed that no heat transfer occurred at the top and bottom of the model. Thus, their boundary conditions can be described as Eqs. (20) and (21). In addition, the coupled boundary condition at the interfaces between the working fluids in the horizontal pipes and tube walls can be defined by Eq. (22).

$$\lambda_{\text{top}} \frac{\partial T}{\partial z}\Big|_{z=0(0\le r\le r_e)} = 0 \tag{20}$$

$$\lambda_{\text{bottom}} \frac{\partial T}{\partial z}\Big|_{z=z_{\max(0\le r\le r_e)}} = 0 \tag{21}$$

$$\begin{cases} \lambda_f \frac{\partial T}{\partial z}|_{z=z_b}(0 < r < r_e) = \lambda_s \frac{\partial T}{\partial z}|_{z=z_b}(0 < r < r_e) \\ T_{\text{hbf}}|_{z=z_b} = T_{\text{hbs}}|_{z=z_b} \end{cases} \tag{22}$$

where λ_{top} and λ_{bottom} are the medium thermal conductivity of the upper boundary and lower boundary, λ_{f} *and* λ_{s} are the thermal conductivity of working fluid and impermeable media, T_{hbf} and T_{hbs} are the working fluid temperature and horizontal pipe temperature at the horizontal pipe/working fluid interface, r_e is the radial distance from the left boundary to the right, and $z_{\max}$ is the total well depth from the surface.

Results and discussion

Based on the information provided above, in this part, the numerical solutions of the four exploitation modes are obtained and discussed in detail. In addition, based on the study of type curves, the sensitivities of the three main categories of factors were analyzed: (a) reinjection parameters, (b) wellbore structure and materials, and (c) geological factors. The coefficients of variation of the outlet temperatures corresponding to various sensitivity parameters were also calculated. Appendix B lists the basis parameters used for calculation. In addition, the transient thermophysical parameters (ρ_{f}, c_{f}, and λ_{f}) of the working fluids (water/SCCO) were obtained by dynamically invoking the database of NIST.

Maximum outlet temperature and type curve analysis of different exploitation modes

To study the optimal outlet temperature for the different exploitation modes, we simulated the outlet temperatures (t_{exp}: 1.0 year) of different q_{in}. To understand complex heat exchanging process for different exploitation modes more conveniently, P_1–P_6 are marked in Fig. 2, and their meanings are as follows: P_1 represents the temperature of injection fluid at the wellhead; P_2 represents the fluid temperature when it enters the horizontal segment from the vertical segment; P_3 is the fluid temperature at the bottom of the horizontal segment of the pipe; P_4 indicates the fluid temperature when it enters the vertical segment from the horizontal segment; In the Model A, P_5 represents the production fluid temperature at the wellhead, however, P_5 represents the fluid temperature at the interface between the HDR and the insulation formation when the produced fluid migrates upward in the Model B; P_6 represents the production fluid temperature at the wellhead in the Model B.

(1) As shown in Fig. 2a–d, for the four exploitation modes, the outlet temperatures all increased first and then decreased with the increase in q_{in}. For any mode, the q_{best} maximizes the outlet temperature (T_{rmax}).

The above phenomenon can be explained as follows (Fig. 2e–h): when the q_{in} is extremely low, the heat loss is excessive in the P_3-P_4-P_5 ([Model A]) or P_5-P_6 ([Model B]) stage although the working fluid can be heated to a higher temperature in the P_1-P_2-P_3 ([Model A]) or P_1-P_2-P_3-P_4-P_5 ([Model B]) stage. In addition, when the q_{in} is extremely high, the heat loss of the working fluid is small in the P_3-P_4-P_5 ([Model A]) or P_5-P_6 ([Model B]) stage. However, the temperature rise is very limited in the P_1-P_2-P_3 ([Model A]) or P_1-P_2-P_3-P_4-P_5 ([Model B]) stage, thus, there is a certain q_{best} leads to T_{rmax}.

In addition, the four exploitation modes had different q_{best}, with values of 339.29 ([Model A, water]), 135.72 ([Model A, SCCO), 542.87 ([Model B, water]), and 271.43 m^3/day ([Model B, SCCO]) and corresponding T_{rmax} of 161.36 °C, 170.80 °C, 134.10 °C, and 152.14 °C, respectively. Therefore, as shown in Fig. 2a–d, i, among all the exploitation modes, [Model A, SCCO] has the highest outlet temperature, and it requires the least amount of fluid injection (q_{best} = 135.72 m^3/day) compared with the other exploitation modes.

(2) During the circulation of the working medium fluid, for [Model A], the working fluid temperature passes through four stages: two stages of temperature rise and two stages of temperature decline. However, for [Model B], the working fluid temperature undergoes five stages: four stages of temperature rise and one stage of temperature decline. The above phenomenon is attributed to the difference in the heat exchange caused by the variation in IPS.

For [Model A] (Fig. 2e–f), when a cooled working fluid is injected into the ANN_V, it will be heated by the surrounding rocks. Then, the working fluid enters the ANN_H and is heated by the HDR around the casing. Therefore, in the annulus (including the vertical and horizontal segments), the working fluid undergoes two stages (P_1–P_2–P_3) of heating. Subsequently, the working fluid enters the TIP_H, because the temperature of the working fluid in the TIP_H is higher than that of the fluid in the ANN_H. Thus, the working fluid transfers heat to the annulus, resulting in its temperature decrease (P_3–P_4). Finally, the working fluid enters the TIP_V. Similarly, the high-temperature working fluid in the TIP_V is cooled by the low-temperature reinjection fluid in the ANN_V, resulting in a decrease in the fluid temperature (P_4–P_5).

For [model B] (Fig. 2g–h), when a cooled working fluid is injected into the TIP_V, the working fluid of the TIP_V will be heated by the high-temperature production fluid in the ANN_V. The working fluid then flows into the TIP_H, which is similarly heated by the fluid in the ANN_H. Thus, the working fluid involves two stages (P_1–P_2–P_3) of heating in the TIP (including the vertical and horizontal segments). Subsequently, the working fluid enters the ANN_H because the temperature of the working fluid in the ANN_H is significantly lower than the ambient temperature (T_b). Hence, the working fluid is continually heated, causing its temperature to rise

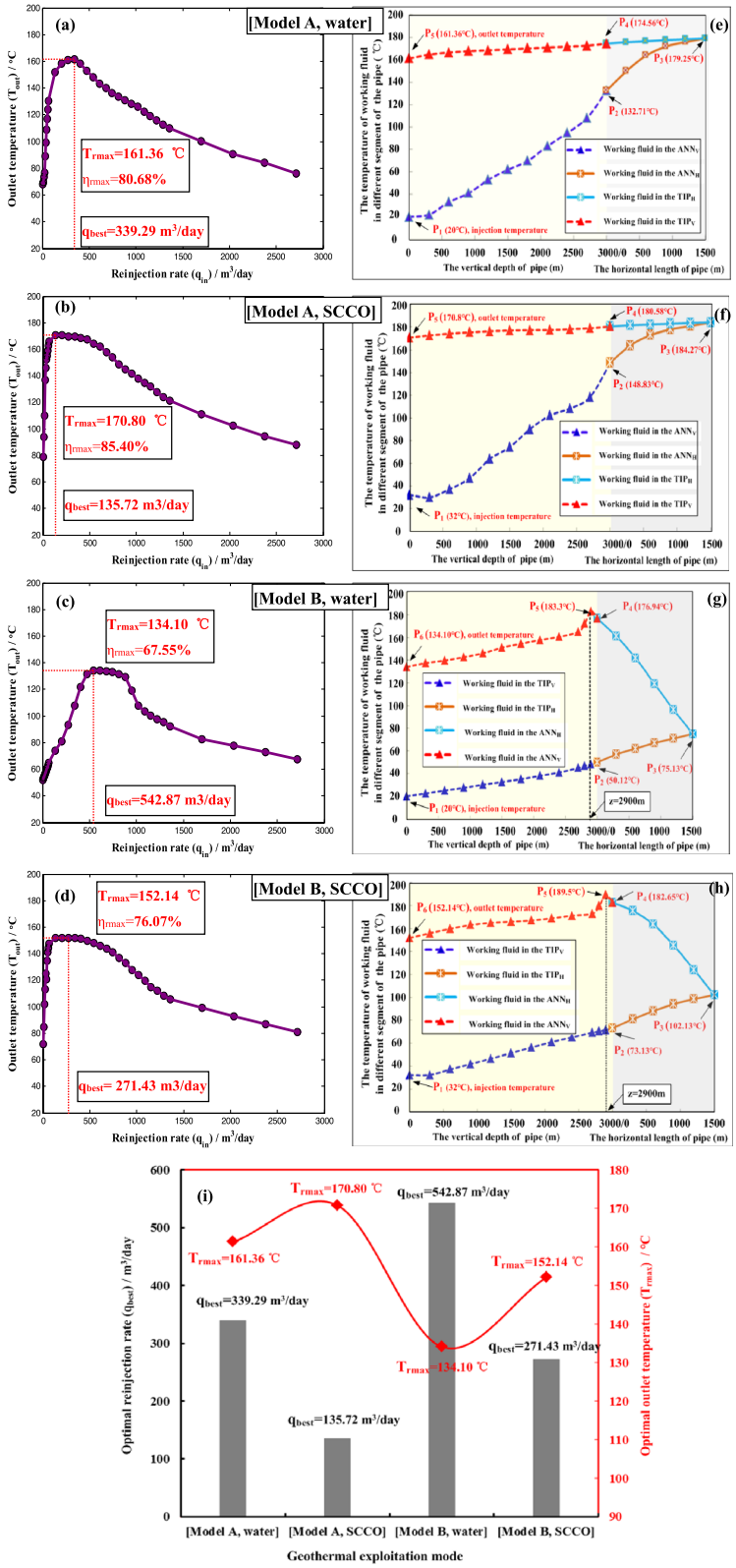

Fig. 2 Comprehensive comparison of the four exploitation modes. **a**–**d** Outlet temperature (t_{exp} = 1.0 year) at different q_{in} for the various exploitation modes. **e**–**h** Type curve analysis of different exploitation modes (t_{exp} = 1.0 year, q_{in} = q_{best}) and the temperature of the working fluid in different segments of the pipe for the various exploitation modes. **i** q_{best} and T_{rmax} for the different exploitation modes (t_{exp} = 1.0 year)

rapidly (P_3–P_4). Finally, the working fluid enters the ANN_V, and given that the temperature of the working fluid at the bottom ($z = 2900$–3000 m) is slightly lower than the T_b of the HDR, the working fluid is also continually heated (P_4–P_5). However, with the upward migration of the working fluid in the ANN_V, its temperature will be higher than that of the surrounding formation and the fluid in the TIP_V. Therefore, the working fluid in the ANN_V transfers heat to the surrounding rock and the TIP_V, resulting in its temperature reduction (P_5–P_6). Thus, in the ANN_V, the working fluid experiences a temperature increase (P_4–P_5) before a temperature decrease (P_5–P_6), which is different from that in [model A].

(3) Under the same conditions, the T_{rmax} of [model A] is greater than that of [model B] because after the working fluid is injected into the annulus, it can be fully heated by the surrounding rock and HDR. Then, the hot working fluid flows into the TIP with a particularly low thermal conductivity (TC). Thus, the working fluid loses less heat, resulting in an increased outlet temperature. However, for [Model B], when a fluid is injected into the TIP, although the working fluid is heated to a high temperature in the TIP (including the vertical and horizontal segments) and the $ANN_{H,}$ given the high TC of the casing and the transition formation/caprock relative to the TIP, the working fluid in the ANN_V will release a large amount of heat to the radial direction (especially in the upper strata). Therefore, the outlet temperature is relatively low. Thus, the use of a low-TC material at the top of the vertical casing can significantly increase the outlet temperature of [Model B].

In addition, under the same IPS, when the working fluid is SCCO, its outlet temperature is greater than that when the working fluid is water because SCCO has a smaller volume heat capacity (VHC) than water and is therefore more easily heated. In addition, SCCO exhibits a relatively minimal heat loss due to its lower TC compared with water. Thus, for geothermal exploitations using a horizontal well, we should attempt to use fluids with low VHC and TC.

Stability comparison of the four geothermal exploitation modes

To compare the stability of the four geothermal exploitation modes, we simulated the outlet temperatures ($q_{in} = q_{best}$) of the different modes at varied t_{exp}. As shown in Fig. 3, for the four exploitation modes, all the outlet temperatures decrease with the t_{exp}, but the outlet temperature change (δT_{out}) in 10 years shows variation ($\delta T_{out} = T_{out}|_{t=10years} - T_{out}|_{t=1year}$). In addition, we defined $|\delta T_{out}|$ as the absolute value of δT_{out} (the same below). In [Model B], the $|\delta T_{out}|$ is significantly greater than that of [Model A], and [Model A, SCCO] is the most stabilized mode with the minimum $|\delta T_{out}|$ of 7.50 °C.

The above phenomenon can be explained as follows: For [Model A], when a working fluid is injected into the ANN_V, it can be continuously heated by the surrounding rock and HDR. Thus, the fluid temperature is relatively high (P_2 in Fig. 2e–f) when the working fluid reaches the ANN_H. Therefore, compared with [Model B], the working fluid absorbs relatively little heat from the HDR around the horizontal pipes in [Model A]. Hence, for [Model A], the T_b of HDR around the ANN_H decreases more slowly than that

in [Model B]. Thus, under the same t_{exp}, the T_b of [Model A] will be high. As a result, the working fluid of [Model A] can be heated to a high temperature before it enters the TIP_V (P_4 in Fig. 2e–f). Thus, the $|\delta T_{out}|$ is small in [Model A] under the same conditions.

Sensitivity analysis of reinjection temperature (T_{in})

Given that the working fluid is constantly exchanging heat with its surrounding environment during circulation, especially in the HDR, a strong heat exchange occurs. Thus, when we studied the sensitivity of T_{in}, the T_b of HDR around the horizontal pipes was considered. Thus, for different T_b, the heat recovery ratio (HRR) ($\eta_s = T_{out}/T_b$) at different T_{in} was simulated. In addition, the effects of T_{in} on the η_s were studied by linear regression analysis (Table 1), and we defined K_{slope} as the slope of η_s with respect to T_{in}.

The following cognitions can be obtained (Fig. 4):

(1) For the four exploitation modes, under any T_b, all η_s increase with the T_{in}, Based on Fourier's first law, with the increase of T_{in}, less heat is released from the working fluid in the vertical output tube into the fluid in the injection tube. Therefore, in the vertical output tube, the temperature of the working fluid decreases relatively less (P_4-P_5 stage for [Model A] and P_5-P_6 stage for [Model B], as shown in Fig. 2e–h).

In addition, as shown in Fig. 4e, the outlet temperature variation ($\Delta T_{sense} = T_{out}|_{Tin=55°C} - T_{out}|_{Tin=15°C}$) decreases with the increase in T_b. However, the ΔT_{sense} is different for the various exploitation modes when T_b is in the range of 74 to 200 °C. For [Model A, water], the ΔT_{sense} drops from 7.85 to 1.47 °C ($K_{solop} = 0.1832–0.0335$); from 5.86 to 1.17 °C ($K_{solop} = 0.1473–0.0259$) for [Model A, SCCO]; from 11.08 to 1.72 °C ($K_{solop} = 0.2771–0.0424$) for [Model B, water]; from 6.81 to 1.30 °C ($K_{solop} = 0.1714–0.0316$) for [Model B, SCCO]. Thus, when the working fluid is water, the effect of T_{in} on η_s is greater than that when the working fluid is SCCO.

(2) In this research, when $K_{slope} \leq 0.05$, the T_{in} has little influence on η_s because when $K_{slope} = 0.05$, when the T_{in} increases/decreases by 40 °C (the T_{in} ranges from 15 to 55 °C), the disturbance of the outlet temperature is at 2% ($0.05\% \times 40 = 2\%$).

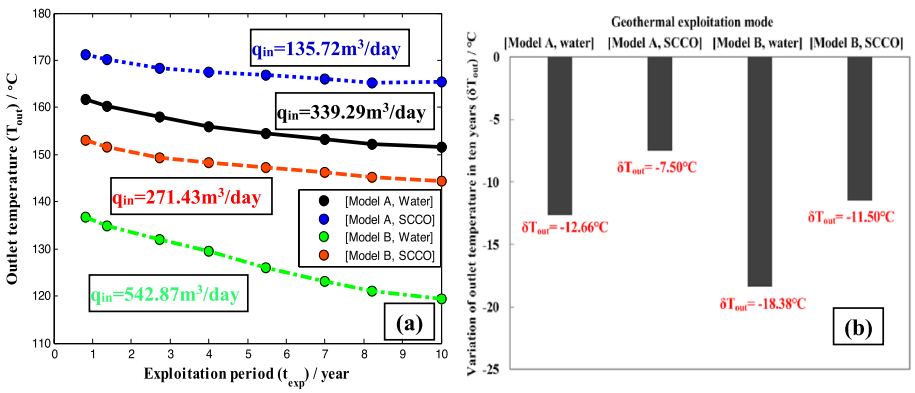

Fig. 3 Stability comparison of the four geothermal exploitation modes. **a** Outlet temperature at different t_{exp} ($q_{in} = q_{best}$). **b** δT_{out} of the different exploitation modes

Table 1 The fitting equations of each curve in Fig. 4

IPS	[Model A, water]	[Model A, SCCO]	[Model B, water]	[Model B, SCCO]
T_b (°C)				
74	$\eta_s = 0.1832\ T_{in} + 65.375$ ($R^2 = 0.987$)	$\eta_s = 0.1470\ T_{in} + 69.375$ ($R^2 = 0.999$)	$\eta_s = 0.2771\ T_{in} + 44.066$ ($R^2 = 0.999$)	$\eta_s = 0.1714\ T_{in} + 61.205$ ($R^2 = 0.999$)
92	$\eta_s = 0.1371\ T_{in} + 68.576$ ($R^2 = 0.997$)	$\eta_s = 0.0913\ T_{in} + 73.948$ ($R^2 = 0.999$)	$\eta_s = 0.1771\ T_{in} + 50.580$ ($R^2 = 0.999$)	$\eta_s = 0.1040\ T_{in} + 65.787$ ($R^2 = 0.998$)
104	$\eta_s = 0.1001\ T_{in} + 71.502$ ($R^2 = 0.992$)	$\eta_s = 0.0530\ T_{in} + 77.576$ ($R^2 = 0.983$)	$\eta_s = 0.1300\ T_{in} + 54.421$ ($R^2 = 0.999$)	$\eta_s = 0.0804\ T_{in} + 68.681$ ($R^2 = 0.999$)
116	$\eta_s = 0.0830\ T_{in} + 73.167$ ($R^2 = 0.988$)	$\eta_s = 0.0502\ T_{in} + 79.456$ ($R^2 = 0.998$)	$\eta_s = 0.1056\ T_{in} + 57.013$ ($R^2 = 0.999$)	$\eta_s = 0.0591\ T_{in} + 70.839$ ($R^2 = 0.999$)
146	$\eta_s = 0.0390\ T_{in} + 77.263$ ($R^2 = 0.989$)	$\eta_s = 0.0328\ T_{in} + 81.646$ ($R^2 = 0.995$)	$\eta_s = 0.0473\ T_{in} + 60.900$ ($R^2 = 0.999$)	$\eta_s = 0.0364\ T_{in} + 73.328$ ($R^2 = 0.997$)
200	$\eta_s = 0.0335\ T_{in} + 79.173$ ($R^2 = 0.952$)	$\eta_s = 0.0259\ T_{in} + 84.373$ ($R^2 = 0.939$)	$\eta_s = 0.0424\ T_{in} + 64.508$ ($R^2 = 0.999$)	$\eta_s = 0.0316\ T_{in} + 74.385$ ($R^2 = 0.980$)

Therefore, the degree of influence is extremely low when $K_{slope} \leq 0.05$. On the contrary, when $K_{slope} > 0.05$, the T_{in} has a relatively large influence on η_s. Thus, when $T_b > 146$ °C, the $K_{slope} < 0.05$ for the four exploitation modes. Therefore, in the geothermal exploitation of horizontal well, when the T_b of stratum reaches 146 °C, the T_{in} has almost no influence on η_s.

Sensitivity analysis of the TC (λ_{TIP}) of the TIP

Figure 5 shows the HRR ($\eta_s = T_{out}/200$ °C, the same below) at different λ_{TIP}. The following cognitions can be obtained:

(1) For the four exploitation modes, their HRR all decrease with the increase in λ_{TIP} because as the λ_{TIP} increases, the working fluid in the output pipe releases more heat. As a result, the fluid temperature drops increasingly during this stage (P_4-P_5 stage for [Model A] and P_5-P_6 stage for [Model B], as shown in Fig. 2e–h).

(2) In this section, we define the temperature variation (ΔT_{sense}) as $\Delta T_{sense} = T_{out}|_{\lambda_{TIP}=46W/(mK)} - T_{out}|_{\lambda_{TIP}=0W/(mK)}$, the $|\Delta T_{sense}|$ (same as below) is the absolute value of ΔT_{sense}. ΔT_{sense} represents the difference between the maximum outlet temperature and the minimum outlet temperature within the variation range of the sensitivity parameter. Thus, the influence degree of λ_{TIP} on the outlet temperature can be ranked from strong to weak as follows (Fig. 5b): $|\Delta T_{sense}| = 40.53$ °C ([Model A, water]) > $|\Delta T_{sense}| = 32.23$ °C (Model B, water) > $|\Delta T_{sense}| = 27.85$ °C ([Model A, SCCO]) > $|\Delta T_{sense}| = 20.76$ °C (Model B, SCCO).

Thus, in [Model A], the disturbance of λ_{TIP} to the HRR is significantly greater than that in [Model B]. However, as shown in Fig. 5a, in [model A], a sudden drop in the HRR occurs when $\lambda_{TIP} > 0$. For [Model A, water], the HRR plummets from 89.63 to 80.31% and from 92.14 to 85.40% for [Model A, SCCO]. Such a phenomenon transpires because for [model A], if the TIP is fully adiabatic ($\lambda_{TIP} = 0$), theoretically, the

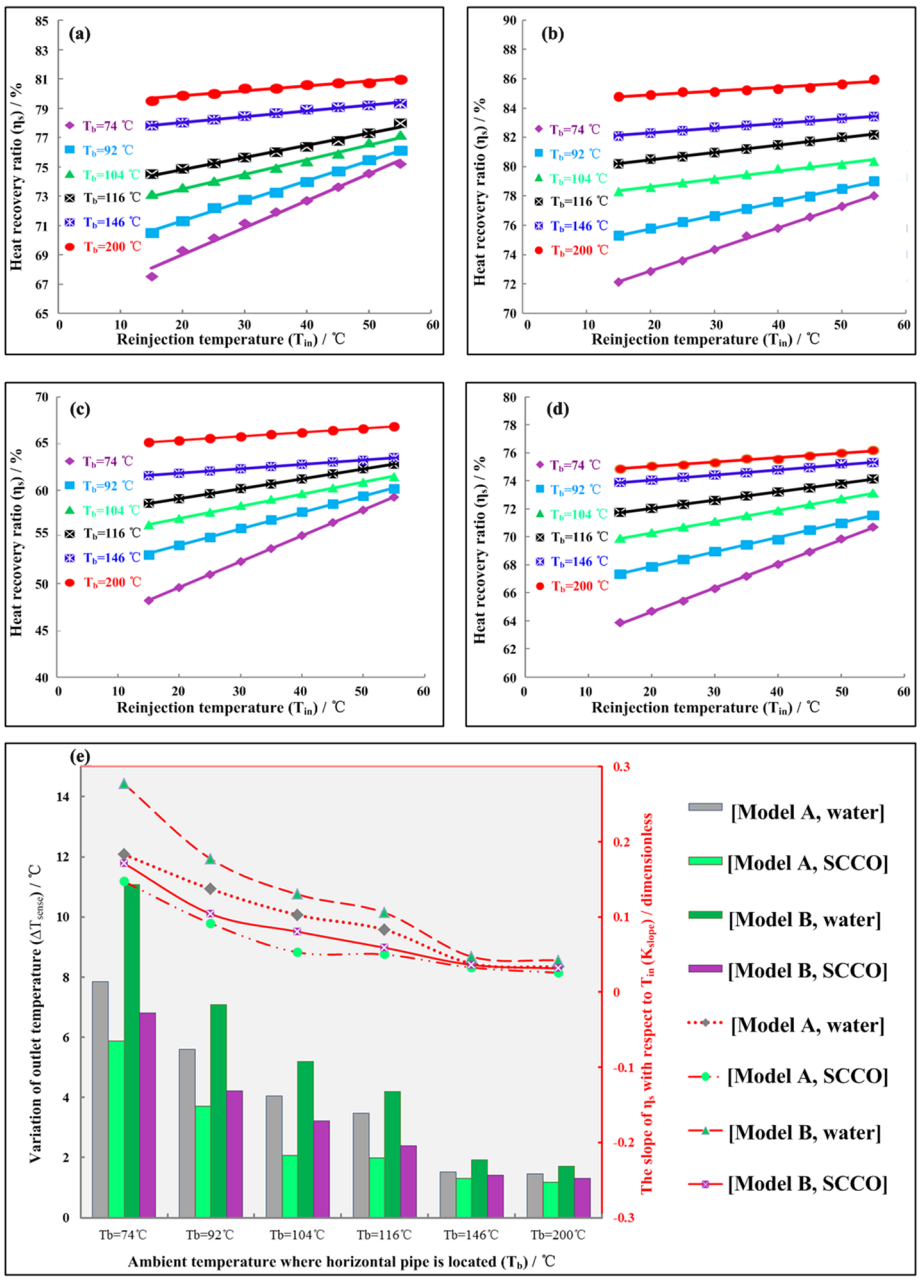

Fig. 4 Sensitivity analysis of T_{in}. **a**–**d** η_s (t_{exp} = 1.0 year) of different T_{in} at various T_b for the four exploitation modes. **e** ΔT_{sense} and K_{slope} at different T_b for the four exploitation modes (t_{exp} = 1.0 year)

working fluid will experience no heat loss in the TIP (P_3-P_4-P_5 stage in Fig. 2e–f). However, for $\lambda_{TIP} > 0$, a certain amount of heat will be lost. As a result, a sharp drop in the HRR will occur.

However, for [Model B], the working fluid in the ANN_V not only releases heat to the reinjection fluid in the TIP_V but also transfer a large amount of thermal energy to the transition formation/caprock. Thus, the heat released by the working fluid in the ANN_V and then into the TIP_V is only a fraction of the total heat loss (P_5-P_6 stage in

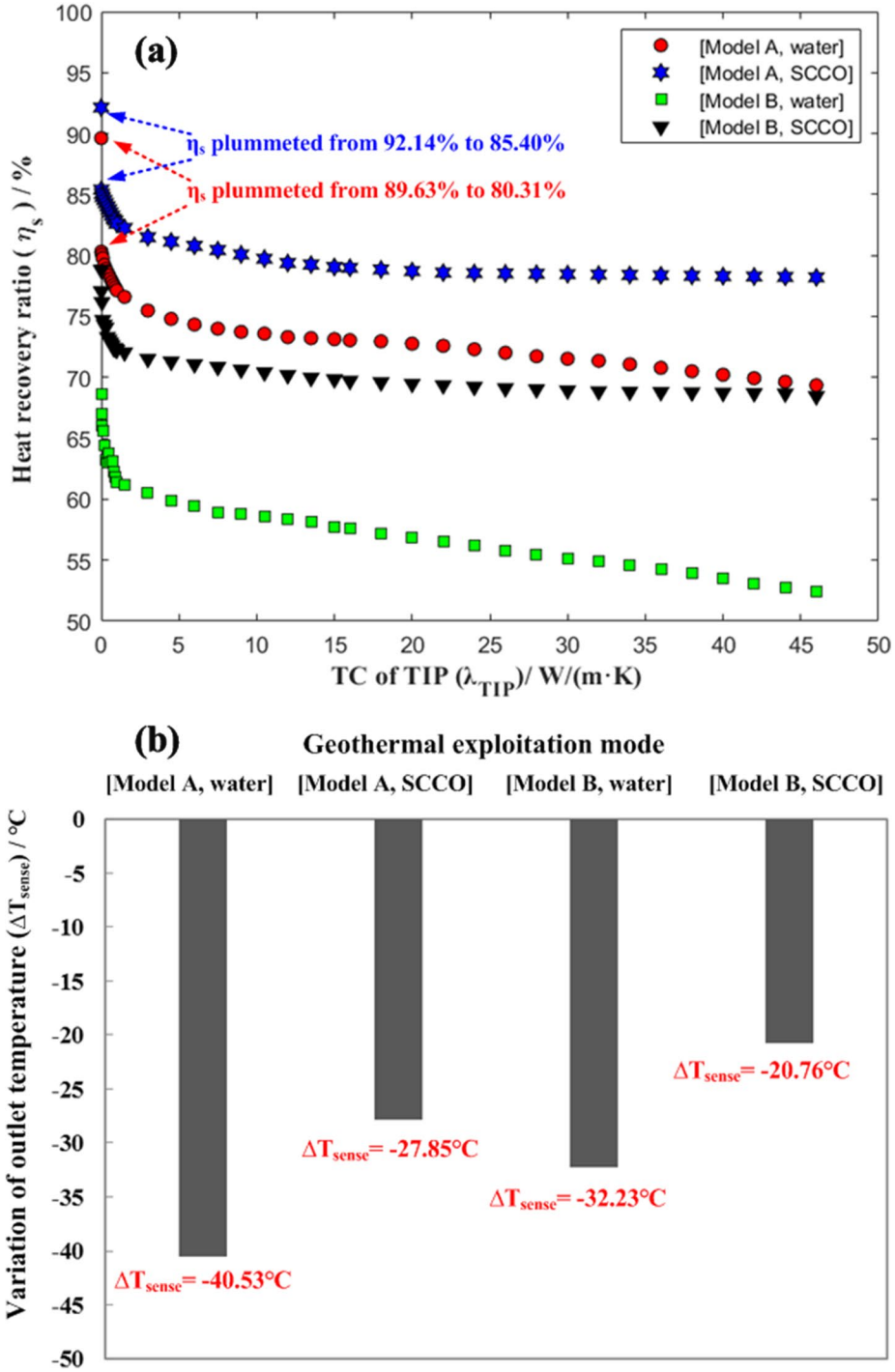

Fig. 5 Sensitivity analysis of λ_{TIP} for the four exploitation modes. **a** HRR (t_{exp} = 1.0 year, $q_{in} = q_{best}$) at different λ_{TIP} for the four exploitation modes. **b** ΔT_{sense} (t_{exp} = 1.0 year, $q_{in} = q_{best}$) of the different exploitation modes

Fig. 2g–h), which is notably different from [Model A] whose working fluid in the TIP_V only releases heat to the ANN_V. Therefore, in [Model B], with the increase in λ_{TIP}, the heat dissipation of the working fluid causes relatively little disturbance to the total

loss of heat. Thus, as shown in Fig. 5a, the HRR only presents a gradually decreasing trend with the increase in λ_{TIP}, and no precipitous drop occurs for [Model B]. In addition, the above reasons explain why the λ_{TIP} has a larger effect on the HRR in [Model A].

Sensitivity analysis of the length (L_{TIP}) of the TIP

Figure 6 shows the HRR of different L_{TIP} for the four exploitation modes. The following cognitions can be obtained:

(1) For the four exploitation modes, their outlet temperatures are positively correlated with the L_{TIP}. However, the outlet temperatures do not increase indefinitely but eventually reach a stable state. In addition, the outlet temperature increases quickly first and then at a lower rate with the increase in L_{TIP}.
(2) Within the variation range (L_{TIP} = 100–2500 m) of the sensitivity parameter, if the difference ($\Delta\eta = \eta_s|_{L_{TIP}=2500m} - \eta_s|_{L_{TIP}=L_{best}}$) between the maximum HRR (L_{TIP} = 2500 m) and the HRR at a certain length (L_{best}) is less than 1% ($\Delta\eta < 1\%$), the HRR can reach the optimal level at that length (L_{best}). In other words, the increase in the L_{TIP} (when $L_{TIP} > L_{best}$) has little effect on the HRR. Hence, as shown in Fig. 6b, the corresponding L_{best} differs for the four exploitation modes, with values of 900 ([Model A, water]), 600 ([Model A, SCCO]), 1200 ([Model B, Water]), and 800 m ([Model B, SCCO]).

Therefore, for [Model A], the L_{best} is significantly shorter than that of [model B] because under the same conditions, for [Model A], when the working fluid reaches the horizontal segment of the pipe, its temperature (P_2 in Fig. 2e–f) is significantly higher than that of [Model B]. Therefore, when the L_{TIP} is shorter, the working fluid can also be sufficiently heated to achieve the optimal outlet temperature. On the contrary, [Model B] needs a longer horizontal pipe to achieve the optimal outlet temperature. This requirement also explains why the outlet temperature of [model B] is more affected by the L_{TIP} compared with [model A]: ΔT_{sense} = 35.69 °C ([Model B, water]) > ΔT_{sense} = 32.39 °C ([Model B, SCCO]) > ΔT_{sense} = 22.25 °C ([Model A, water]) > ΔT_{sense} = 18.68 °C ([Model A, SCCO]). In this section, we define the temperature variation (ΔT_{sense}) as $\Delta T_{sense} = T_{out}|_{L_{TIP}=2500m} - T_{out}|_{L_{TIP}=100m}$.

Sensitivity analysis of geological thermophysical parameters

The correlation between the outlet temperature and different formations of thermophysical parameters is seriously affected by the IPS and t_{exp}. These formations include the caprock, transition formation, and HDR, which are summarized in Table 2.

[+,−] indicates that in the early stage of exploitation, the outlet temperature is positively correlated with the studied parameter, whereas in the later stage of exploitation, the outlet temperature is negatively correlated with the studied parameter. [+] represents that the outlet temperature is always positively correlated with the studied parameter. [−] denotes that the outlet temperature is always negatively correlated with the studied parameter.

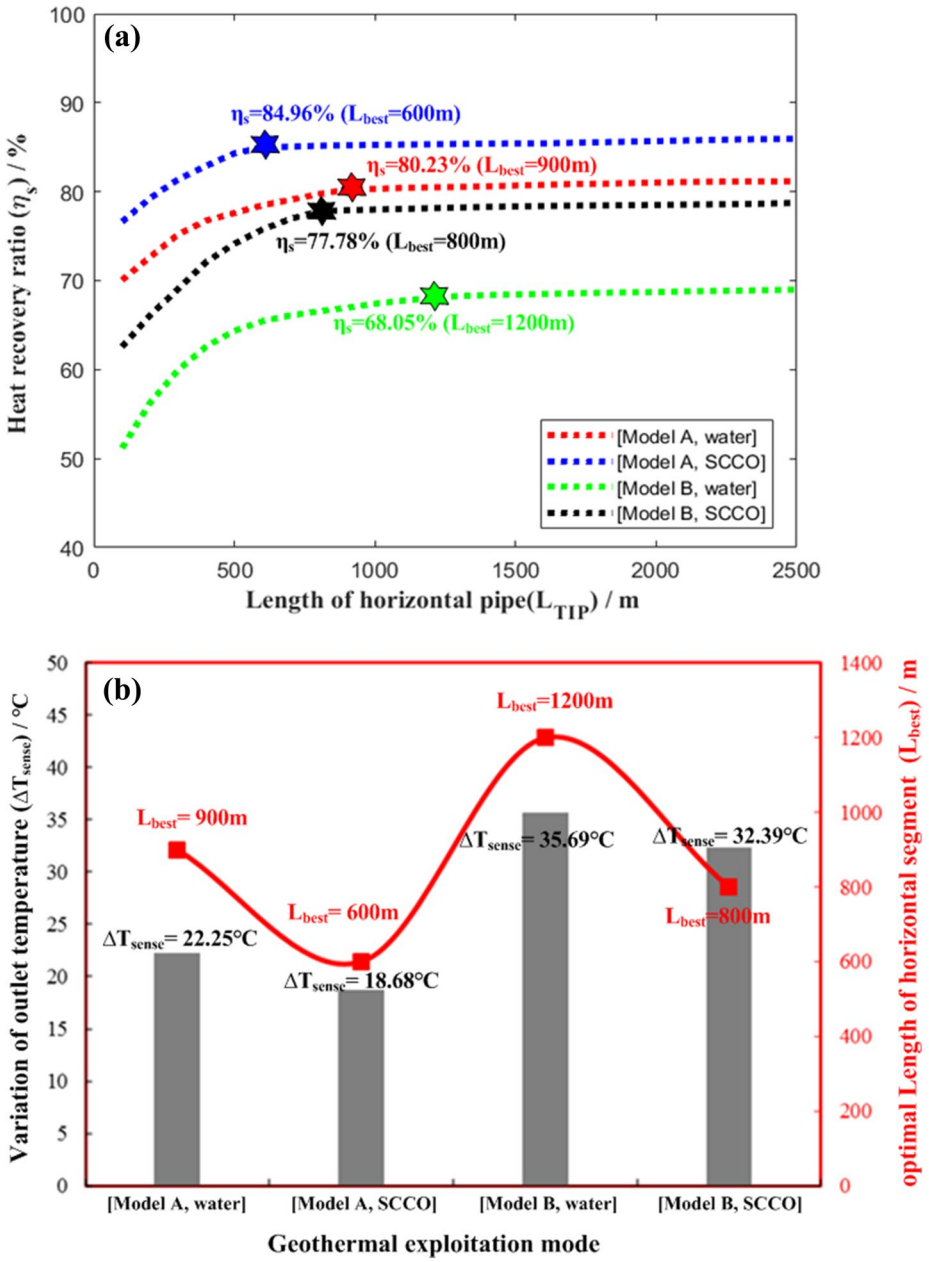

Fig. 6 Sensitivity analysis of the L_{TIP} for the four exploitation modes. **a** HRR ($t_{exp} = 1.0$ year, $q_{in} = q_{best}$) with different L_{TIP} for the four exploitation modes. **b** ΔT_{sense} and L_{best} of different exploitation modes ($t_{exp} = 1.0$ year, $q_{in} = q_{best}$)

Sensitivity analysis of the transition formation

Figure 7 shows the HRR with different λ_{tran} at various t_{exp} for the four exploitation modes. The following cognitions can be obtained:

(1) In [Model A], the correlation between the HRR and the λ_{tran} differs at various t_{exp}. As shown in Fig. 7a–b, e, in this study, when $t_{exp} \leq 3.0$ years, the HRR is positively correlated with the λ_{tran}. However, when $t_{exp} \geq 5.0$ years, the HRR is inversely correlated with the λ_{tran}. However, when this correlation changes, the t_{exp} may vary depending

Table 2 Changes in the correlation between the outlet temperature and geological thermophysical parameters under different IPS and t_{exp}

Stratum	Geological parameter	[Model A]	[Model B]	Model whose outlet temperature is more affected under the same correlation
Transition formation	λ_{trans}	[+,−]	[−]	/
	VHC_{trans}	[+]	[−]	/
HDR	λ_{HDR}	[+,−]	[+,−]	[Model B]
	VHC_{HDR}	[+]	[+]	[Model B]

on the model parameters (or actual geological setting parameters). The reasons for the changes in the correlation between the HRR and the λ_{tran} are as follows.

In the early stage of exploitation, for [Model A], with the increase in the λ_{tran}, the transition formation becomes more favorable to heat the working fluid in the ANN_V (P_1-P_2 stage in Fig. 2e–f; depth range: $z = 200$–2800 m). Therefore, when the working fluid reaches the ANN_H, the temperature is high (P_2 in Fig. 2e–f). Thus, the outlet temperature is also high. However, given that the transition formation continuously transfers heat to the upper stratum, over time (especially in the late stage of exploitation), the greater the λ_{tran}, the more heat is transferred to the upper stratum from the lower stratum. This condition leads to a decrease in the T_b of the transition formation ($z = 200$–2800 m), which lowers the temperature (P_3 in Fig. 2e–f) of the working fluid when it enters the TIP_H, thus resulting in a decrease in the HRR. Therefore, in the early stage of exploitation, the HRR increases with the λ_{tran}, whereas in the later stage of exploitation, the HRR decreases.

(2) However, for [Model B], as shown in Fig. 7c–d, e, given the large λ_{tran}, the fluid in the ANN_V releases more heat to the surrounding rock, especially in the upper part of the transition formation (P_5-P_6 stage in Fig. 2g–h). Therefore, as shown in Fig. 7e, the HRR consistently decreases with the λ_{tran}, but the $|\Delta T_{sense}|$ gradually decreases over time. In this section, we define the temperature variation (ΔT_{sense}) as $\Delta T_{sense} = T_{out}|_{\lambda_{tran}=6W/(mK)} - T_{out}|_{\lambda_{tran}=0.9W/(mK)}$.

Figure 8 shows the HRR with different VHC_{tran} for the four exploitation modes. The following cognitions can be obtained:

(1) For [model A], the fluid in the ANN_V continuously absorbs heat from the surrounding rock. Therefore, as mentioned above, under the same conditions, the larger the VHC_{tran}, the more heat the surrounding rock will release. Thus, the working fluid in the ANN_V can absorb more heat. This condition allows the working fluid to have a higher temperature (P_3 in Fig. 2e–f) before entering the TIP_H. As a result, the outlet temperature increases. Similarly, in the later stage of exploitation development, the larger the VHC_{tran}, the more thermal energy exists in the reservoir, especially around the depth ($H = 3000$ m) where the horizontal pipe is located. Hence, the outlet tem-

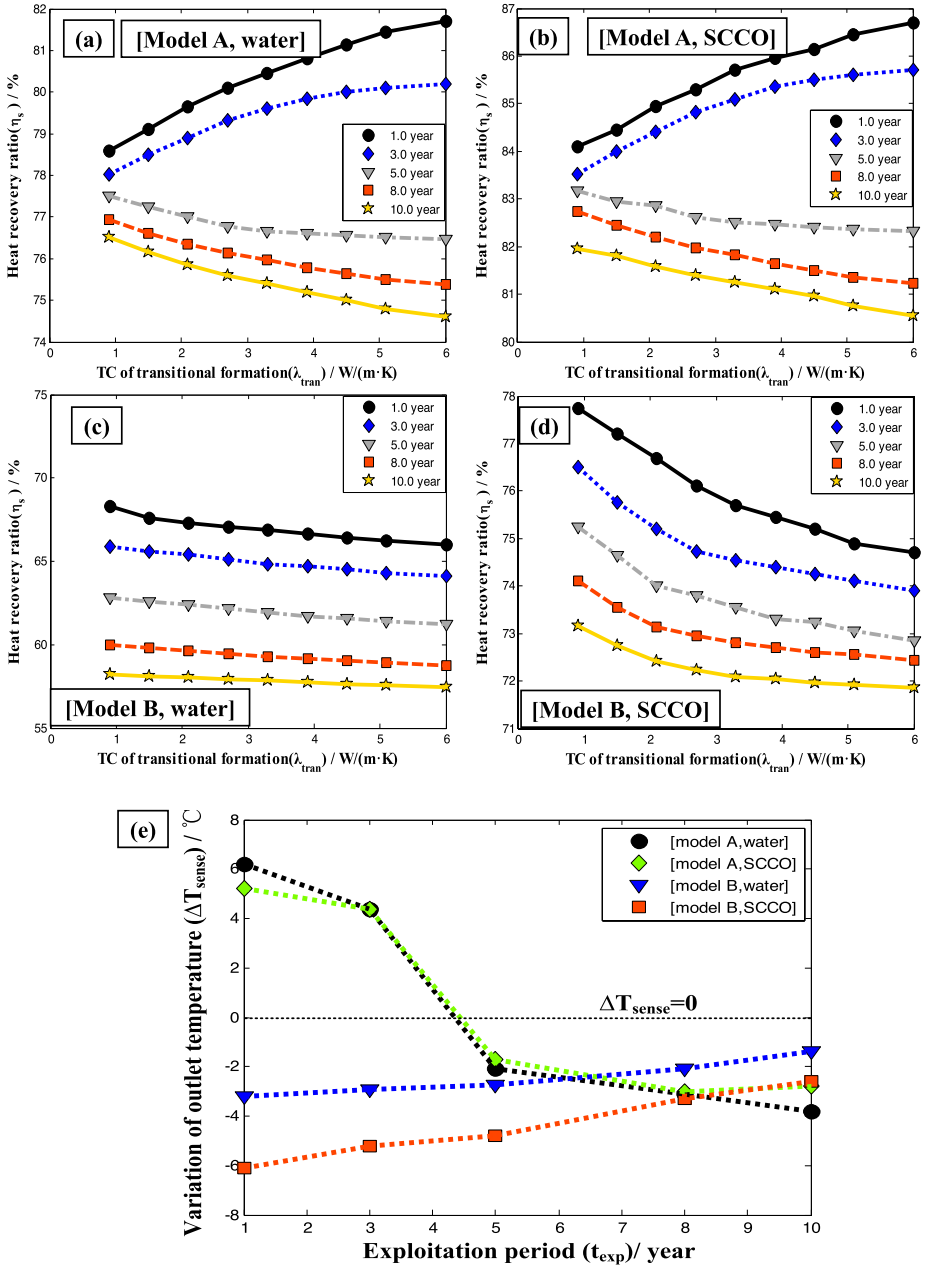

Fig. 7 Sensitivity analysis of the λ_{tran} at different t_{exp} for the four exploitation modes. **a**–**d** HRR ($q_{in} = q_{best}$) with different λ_{tran} at various t_{exp} for the four exploitation modes. **e** ΔT_{sense} ($q_{in} = q_{best}$) at different t_{exp} for the different exploitation modes

perature will also be higher. Thus, for [Model A], in the whole exploitation process, the HRR is always positively correlated with the VHC_{tran}.

In addition, the above factors explain why the influence of VHC_{tran} on the outlet temperature becomes more significant with the t_{exp} over a period of 1–10 years. The temperature variation ($\Delta T_{sense} = T_{out}|_{VHC_{tran}=4.5\times10^6 J/(m^3\cdot K)} - T_{out}|_{VHC_{tran}=0.6\times10^6 J/(m^3\cdot K)}$)

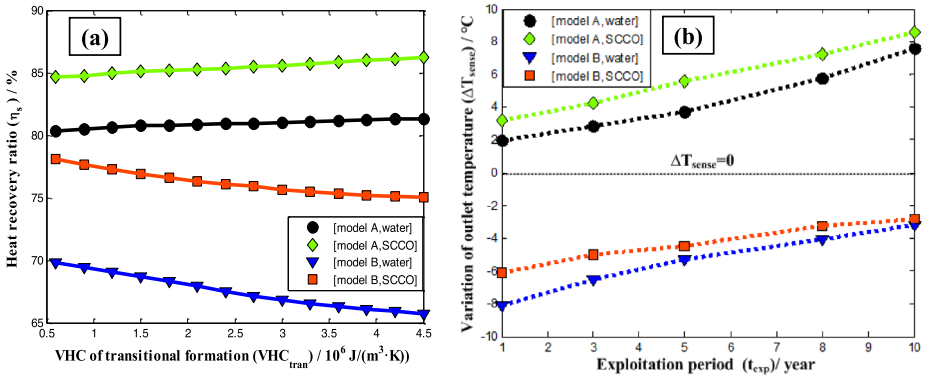

Fig. 8 Sensitivity analysis of the VHC_{tran} for the four exploitation modes. **a** HRR (t_{exp} = 1.0 year, q_{in} = q_{best}) with different VHC_{tran} for the four exploitation modes. **b**) ΔT_{sense} (q_{in} = q_{best}) at different t_{exp} for the various exploitation modes

increases from 2.28 to 7.88 °C for [Model A, water] and increases from 3.70 to 10.06 °C for [Model A, SCCO].

(2) However, for [Model B], a large VHC_{tran} will lead to the increased heat release of the working fluid in the ANN_V (P_5-P_6 stage in Fig. 2g–h). Under the same conditions, if the VHC_{tran} is large, then the temperature of the surrounding rock increases by 1 °C, and the surrounding rock needs to absorb more heat from the working fluid in the ANN_V. Therefore, the temperature of the working fluid decreases more during this stage (P_5-P_6 in Fig. 2g–h). Thus, the HRR is always inversely correlated with the VHC_{tran}. In addition, as shown in Fig. 8b, the $|\Delta T_{sense}|$ also decreases with the t_{exp}, the principle is similar to that of the VHC_{cap} above.

Sensitivity analysis of the HDR

As shown in Fig. 9a–d, for the four exploitation modes, the correlation between the HRR and λ_{HDR} differs at various t_{exp}. In this study, when $t_{exp} \leq 3.0$ years, the HRR is positively correlated with the λ_{HDR}. However, when $t_{exp} \geq 5.0$ years, the HRR is inversely correlated with the λ_{HDR}. Still, when this correlation changes, the t_{exp} may vary depending on the model parameters. The reasons for the changes in the correlation between the HRR and λ_{HDR} are as follows.

In the early stage of exploitation, with the increase in the λ_{HDR}, the HDR becomes more favorable to heat the working fluid. Therefore, for [Model A], when the working fluid reaches the TIP_H, the temperature increases (P_3 in Fig. 2e–f). In the same manner, for [Model B], when the working fluid in the ANN_V enters the section of insulation formation (z = 2800–2900 m), the temperature increases (P_5 in Fig. 2g–h). Thus, the HRR increases with the λ_{HDR} in the early stage of exploitation.

However, given that the HDR also continuously transfers heat to the upper stratum and the working fluids, over time (especially in the late stage of exploitation), the greater the λ_{HDR} is, the more heat is lost. This condition leads to a decrease in the T_b of the HDR, which lowers the temperature of the working fluid (for [Model A], the temperature node is P_3 in Fig. 2e–f; for [Model B], the temperature node is P_5 in Fig. 2g–h),

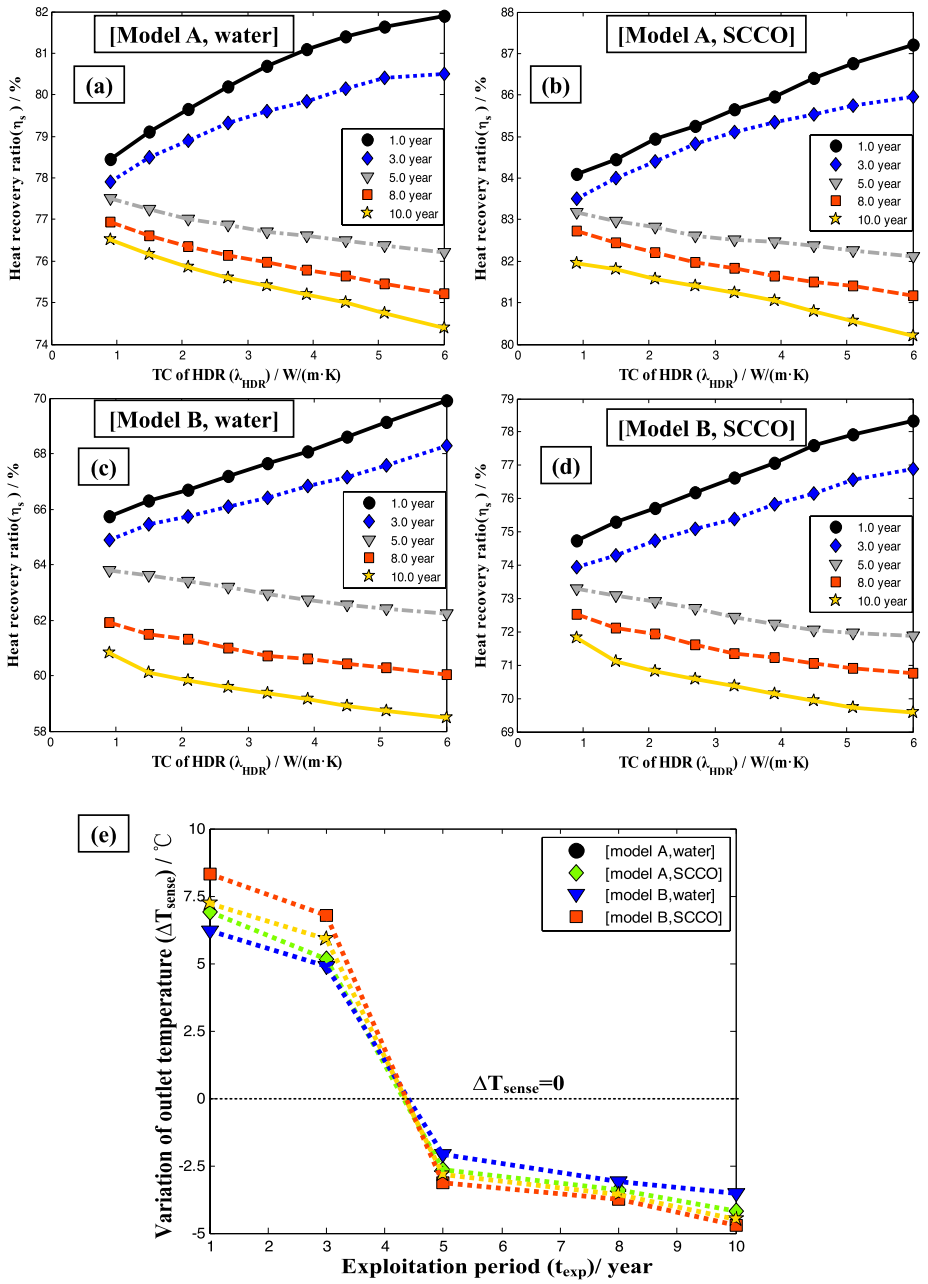

Fig. 9 Sensitivity analysis of the λ_{HDR} at different t_{exp} for the four exploitation modes. **a**–**d** HRR ($q_{in} = q_{best}$) with different λ_{HDR} at various t_{exp} for the four exploitation modes. **e** ΔT_{sense} ($q_{in} = q_{best}$) at different t_{exp} for the various exploitation mode

thus resulting in a decrease in the HRR. Therefore, in the early stage of exploitation, the HRR increases with the λ_{HDR}, whereas in the later stage of exploitation, the HRR decreases. The above factor also explains why the $|\Delta T_{sense}|$ increases with t_{exp} in the late stage of exploitation. In this section, we define the temperature variation (ΔT_{sense}) as:$\Delta T_{sense} = T_{out}|_{\lambda_{HDR}=6W/(mK)} - T_{out}|_{\lambda_{HDR}=0.9W/(mK)}$.

Figure 10 shows the HRR with different VHC_{HDR} for the four exploitation modes. The following cognitions can be obtained:

In the early stage of exploitation, the working fluid in the horizontal segment continuously absorbs heat from the HDR. Therefore, as mentioned above, under the same conditions, the larger the VHC_{HDR}, the more heat the surrounding rock will release, and the more heat the working fluid in the horizontal segment can absorb. Thus, for [Model A], this condition increases the working fluid temperature (P_3 in Fig. 2e–f) before entering the TIP_H. In the same manner, for [Model B], when the working fluid in the ANN_V enters the section of insulation formation ($z = 2900$ m), the temperature also increases (P_5 in Fig. 2g–h). As a result, the HRR increases with the λ_{HDR}. Similarly, in the later stage of exploitation development, the larger the VHC_{HDR} is, the more thermal energy exists in the HDR, especially around the depth ($H = 3000$ m) where the horizontal pipe is located. Hence, the working fluid can be heated to a high temperature. Thus, for the four exploitation modes, in the whole exploitation process, the HRR is always positively correlated with the VHC_{HRD}.

In this section, we define the temperature variation (ΔT_{sense}) as $T_{out}|_{VHC_{HDR}=4.5\times10^6 J/(m^3\cdot K)} - T_{out}|_{VHC_{HDR}=0.6\times10^6 J/(m^3\cdot K)}$. As shown in Fig. 10b, for the different exploitation modes, the all ΔT_{sense} increase with the t_{exp} because with the increase in the t_{exp}, the differences in the VHC_{HRD} lead to greater differences in the heat energy of HDR. As a result, the outlet temperature experiences a greater disturbance.

Comprehensive comparison of sensitivity analysis

To comprehensively compare the influence degree of various parameters on the HRR in this study, based on the principle of mathematical statistics, we adopted the coefficient of variation as the index of sensitivity evaluation (Abdi 2010; McAuliffe 2015):

$$C_v = \frac{s}{|\bar{y}|} \tag{23}$$

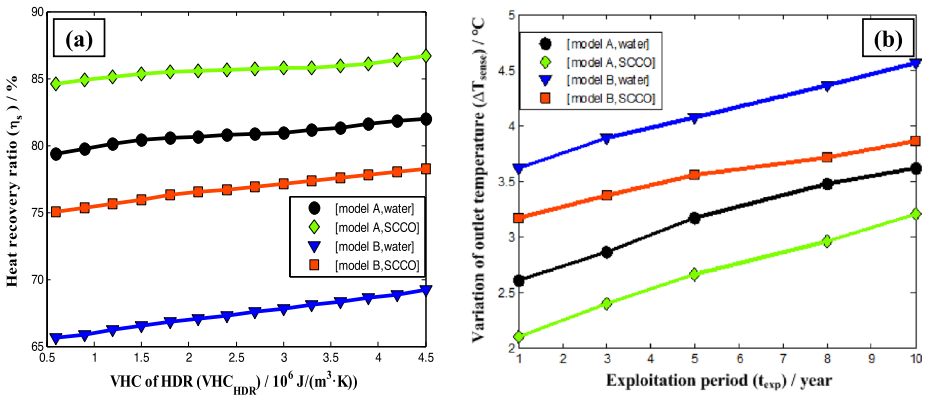

Fig. 10 Sensitivity analysis of the VHC_{HDR} at different t_{exp} for the four exploitation modes. **a** HRR ($t_{exp} = 1.0$ year, $q_{in} = q_{best}$) with different VHC_{HDR} for the four exploitation modes. **b** ΔT_{sense} ($q_{in} = q_{best}$) at different t_{exp} for the various exploitation modes

$$s = \sqrt{\frac{1}{N}\sum_{i=1}^{N}\left(y_i - \bar{y}\right)^2} \tag{24}$$

where C_v is the coefficient of variation, s is the standard deviation of the sample data, $|\bar{y}|$ is the average of sample data, y_i represents a data sample, and N represents the number of sample data.

The value of C_v reflects the sensitivity of HRR to various influencing factors. The greater the C_v value, the greater the influence of this factor on the HRRs. Figure 11 summarizes the results of the sensitivity comparison of the studied parameters. For the four exploitation modes, although the sensitivity of each mode to various parameters varies, in the studied parameter ranges, λ_{TIP} and L_{TIP} have the greatest degree of sensitivity. Thus, the design of the TIP must be optimized. The effect of the T_{in} on the HRR decreases with the increase in T_b. Hence, for the area that meets the HDR standard ($T_b > 150$ °C), the effect of the T_{in} on the HRR can be ignored. In addition, the caprock with a high TC damages the geothermal exploitation performance. However, the correlations between the HRR and thermophysical properties of different formations are seriously affected by the IPS and t_{exp}.

Conclusions

In this study, a fully coupled model was established to synthetically analyze the geothermal exploitation using a horizontal well under different IPS and working fluids. Dynamic optimization analysis was carried out from the space–time perspective. The following conclusions have been drawn:

(1) Under the same conditions, [Model A] is the best IPS because of its high outlet temperature, stable thermal recovery, and low fluid injection volume. If [Model B]

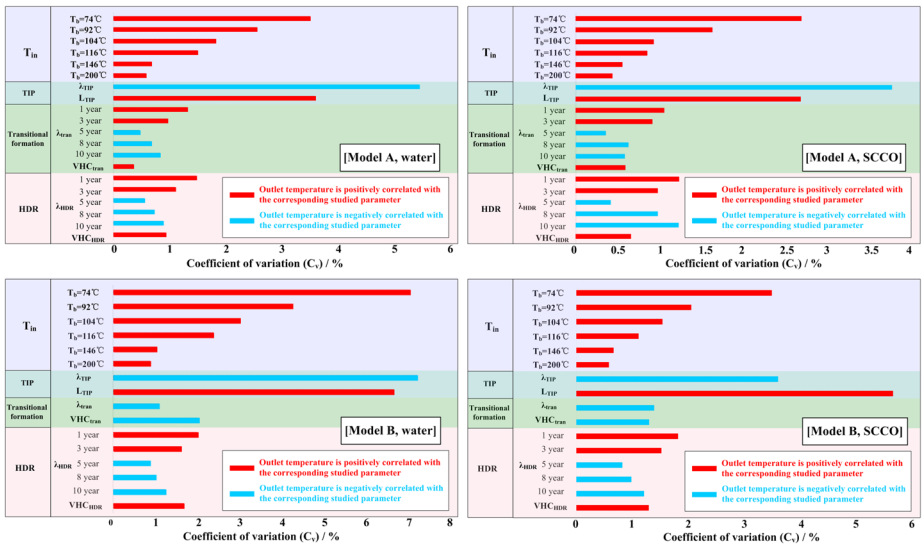

Fig. 11 Coefficient of variation of the outlet temperature corresponding to various sensitivity parameters for the four exploitation modes

must be adopted as the exploitation scheme, the casing pipe in the upper part of the formation should be made of materials with a low TC. Moreover, for any IPS, when a fluid (e.g., SCCO) with low VHC and TC is used as the working fluid, its HRR will be notably high.

(2) Type curve analysis shows that: (a) For [Model A], the working fluid temperature passes through four stages (two stages of temperature rise and two stages of temperature decline); (b) For [Model B], the working fluid temperature undergoes five stages (four stages of temperature rise and one stage of temperature decline).

(3) When the T_b exceeds 146 °C, the T_{in} has almost no influence on the outlet temperature (with the increase in the T_{in}, the outlet temperature disturbance remains below 1%). Therefore, for the area that meets the HDR standard ($T_b > 150$ °C), the effect of the T_{in} on the outlet temperature can be ignored. In addition, each mode has an optimal q_{best} (a maximum outlet temperature exists in the relation curve between the outlet temperature and q_{in}), which varies depending on the IPS and the working fluid.

(4) The TIP properties seriously affect the HRR: (a) The study of variation coefficient showed that among all the sensitivity parameters studied in this research, λ_{TIP} and L_{TIP} have the greatest influence on the HRR. Therefore, the materials of TIP must be optimized. (b) For [model A], when $\lambda_{TIP} = 0$, the HRR is the highest; otherwise, the HRR sharply declines. However, in [Model B], regardless of whether the TIP is completely adiabatic, the outlet temperature decreases gradually with λ_{TIP}. Thus, the TIP of completely adiabatic materials ($\lambda_{TIP} = 0$) is a great addition to [Model A]. (c) Given economic considerations, a long horizontal pipe is not optimal. The research showed that the L_{TIP} becomes shorter when [model A] obtains the optimal outlet temperature compared with [model B].

(5) The influence of IPS and t_{exp} should be fully considered when analyzing the influence of different formations of thermophysical parameters on the outlet temperature (Table 1).

(6) The model in this paper does not consider the influence of chemical reaction between the working medium and casing on geothermal development. Therefore, in further research, a fully coupled thermo-hydro-mechanical-chemical model should be constructed to study the dynamic evolution characteristics of thermal extraction during the geothermal development of the horizontal wells. In addition, considering the economic factors of geothermal exploitation will be the key direction of geothermal development numerical simulation optimization research.

Appendix A

In this model, the finite difference method was used to discretize the transient temperature field governing equation. In addition, the mesh at the wellbore location was refined. In the area where the vertical or horizontal well exists, the spacing was set as 0.01 m to describe the temperature precisely. However, the grid with equal spacing of 2.0 m was used for the formations. Figure 12 shows the details of mesh generation.

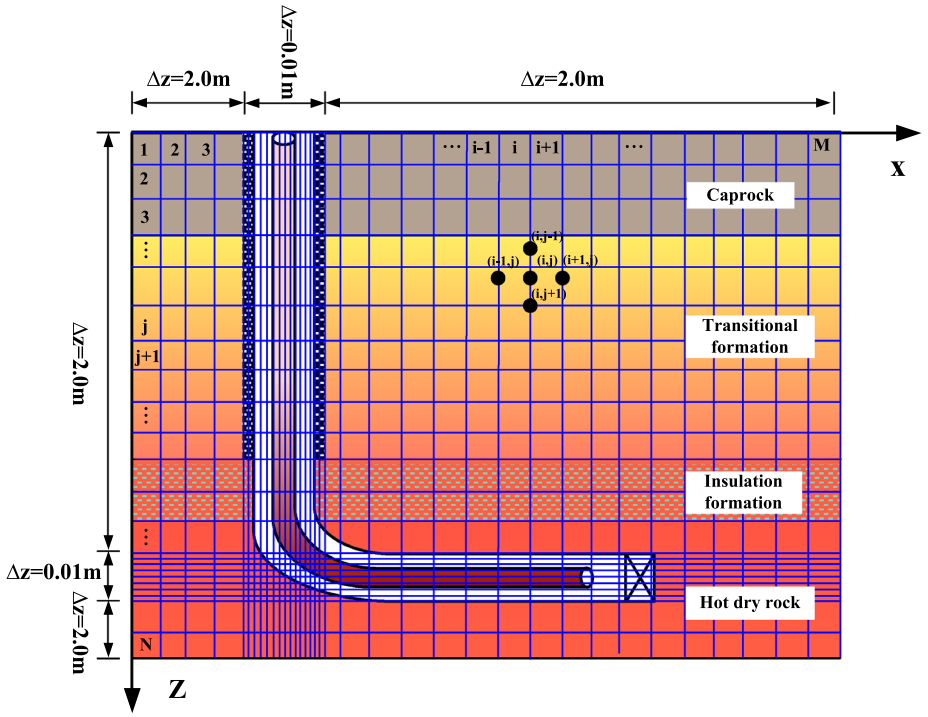

Fig. 12 Schematic of the discrete grid of the model

Appendix B

Tables 3 and 4 list the parameters of the base model using the horizontal well technology for the geothermal exploitation of HDR. Figure 13 shows the initial T_b of the model. When the working fluid is water or SCCO, the reinjection temperature is 20 °C and 32 °C, respectively. In the sensitivity analysis, the volume reinjection rate of each model was set to the optimal values): 339.39 ([Model A, water]), 135.72 ([Model A, SCCO]), 542.87 ([Model B water]), and 271.43 m^3/day ([Model B, SCCO]).

Table 3 Geometry parameters of the wellbore

Length of vertical well (L_{TIP}), m	3000
Length of horizontal well (L_{ver}), m	1500
The total depth of the model (z_{max}), m	3100
Inner diameter of thermal insulation pipe (D_{Inn}), m	0.2
Thickness of thermal insulation pipe (D_{TIP}), m	0.02
Radial spacing of annulus (D_{Ann}), m	0.04
Thickness of casing (D_{Cas}), m	0.02
Thickness of cement sheath (D_{Cs}), m	0.02

Table 4 Thermo-physical properties of various media

Volumetric heat capacity of thermal insulation pipe (VHC_{TIP}), J/(m^3 K)	3.63×10^6
Volumetric heat capacity of casing (VHC_{cas}), J/(m^3 K)	3.63×10^6
Volumetric heat capacity of cement sheath (VHC_{cs}), J/(m^3 K)	1.85×10^5
Volumetric heat capacity of caprock (VHC_{cap}), J/(m^3 K)	1.96×10^6
Volumetric heat capacity of transition formation (VHC_{tf}), J/(m^3 K)	2.10×10^6
Volumetric heat capacity of insulation formation (VHC_{if}), J/(m^3 K)	2.3×10^6
Volumetric heat capacity of hot dry rock (VHC_{HDR}), J/(m^3 K)	2.60×10^6
Thermal conductivity of thermal insulation pipe (λ_{TIP}), W/(m K)	0.03
Thermal conductivity of casing (λ_{cas}), W/(m K)	45
Thermal conductivity of cement sheath (λ_{cs}), W/(m K)	22
Thermal conductivity of caprock (λ_{cap}), W/(m K)	2.1
Thermal conductivity of transition formation (λ_{tran}),W/(m K)	2.8
Thermal conductivity of insulation formation (λ_{if}),W/(m K)	0.3
Thermal conductivity of hot dry rock reservoir (λ_{HDR}),W/(m K)	2.6

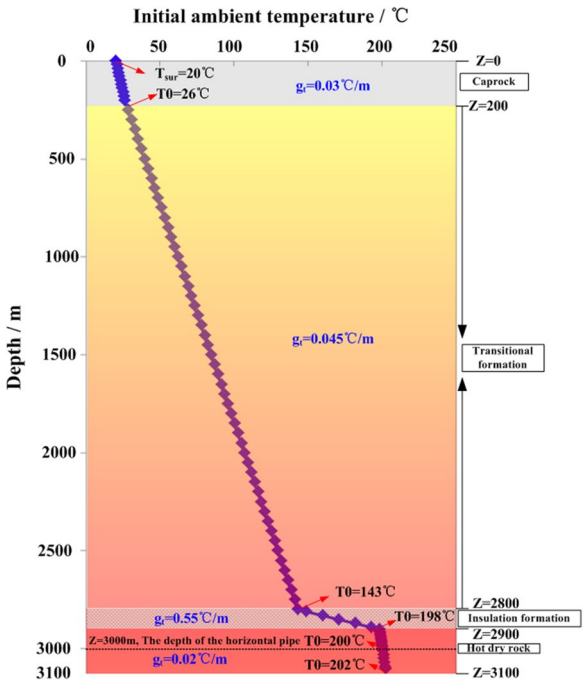

Fig. 13 Initial T_b of the model

Abbreviations

c_f	Specific heat capacity of the working fluid, J/(kg K)
c_s	Specific heat capacity of the impermeable media, J/(kg·K)
C_v	Coefficient of variation, %
D_{Ann}	Radial spacing of annulus, m
D_{Cas}	Thickness of casing, m
D_{Cs}	Thickness of cement sheath, m
D_{inn}	Inner diameter of thermal insulation pipe, m
D_{TIP}	Thickness of the thermal insulation pipe, m
g_T	Geothermal gradient, °C/m
h_c	Convection heat transfer coefficient, W/(m^2·K)
K_{slope}	Slope of η_s with respect to T_{in}, dimensionless

L	Characteristic length in Eq. (19), m
L_{best}	Horizontal length of the thermal insulation pipe when the heat recovery ratio reach the optimal value, m
L_{TIP}	Horizontal length of the thermal insulation pipe, m
L_{ver}	Vertical length of the thermal insulation pipe, m
n	Coefficients in Eq. (19), n = 0.3(when the fluid is heated) or n = 0.2 (when the fluid is cooled)
P_{rf}	Prandtl number, dimensionless
q_{best}	Optimal volumetric reinjection rate, m^3/s
q_{in}	Total volumetric reinjection rate, m^3/s
r_e	Radial distance from the left boundary to the right, m
r_{fp}	Boundary between the working fluid and the vertical pipe, m
r_{vh}	Boundaries between the working fluids in the vertical pipes and working fluids in the horizontal pipes, m
R_{ef}	Reynolds number, dimensionless
s	Standard deviation of the sample data, in Eq. (24)
t_{exp}	Exploitation period, year
T	Temperature at a specific exploitation period, ℃
T_a	Initial ambient temperature, ℃
T_b	Ambient temperature at the depth of horizontal pipe. $T_b = g_T \times L_{ver}$
T_{bp}	Temperature of the vertical pipe at the working fluid/vertical pipe interface, ℃
T_{bf}	Working fluid temperature at the working fluid/vertical pipe interface, ℃
T_{hbf}	Working fluid temperature of the horizontal pipe at the horizontal pipe/working fluid interface, ℃
T_{hbs}	Temperature of the horizontal pipe at the horizontal pipe/working fluid interface, ℃
T_{hf}	Working fluid temperature in the horizontal pipe at the horizontal pipe/vertical pipe interface, ℃
T_{in}	Reinjection temperature, ℃
T_{out}	Outlet temperature, ℃
T_{rmax}	Maximum outlet temperature, ℃
T_{sur}	Initial surface temperature, ℃
T_{vf}	Working fluid temperaturein the vertical pipe at the horizontal pipe/vertical pipe interface, ℃
v_r	Seepage velocity of the working fluid in the horizontal pipes, m/s
v_z	Seepage velocity of the working fluid in the vertical pipes, m/s
VHC_{cap}	Volumetric heat capacity of caprock, $J/(m^3\ K)$
VHC_{cas}	Volumetric heat capacity of casing, $J/(m^3\ K)$
VHC_{cs}	Volumetric heat capacity of cement sheath, $J/(m^3\ K)$
VHC_{HDR}	Volumetric heat capacity of the hot dry rock, $J/(m^3\ K)$
VHC_{if}	Volumetric heat capacity of insulation formation, $J/(m^3\ K)$
VHC_{TIP}	Volumetric heat capacity of thermal insulation pipe, $J/(m^3\ K)$
VHC_{tf}	Volumetric heat capacity of transition formation, $J/(m^3\ K)$
VHC_{tran}	Volumetric heat capacity of the transition formation, $J/(m^3\ K)$
y_i	A data sample
$\overline{y}$	Average of sample data
z	Vertical depth from surface, m
z_b	Depths of the interfaces between the working fluid in the horizontal pipes and the tube wall, m
z_{max}	Total well depth from the surface, m
λ_{bottom}	Thermal conductivity of the medium at the lower boundary of the model, W/(m·K)
λ_{cas}	Thermal conductivity of casing, W/(m·K)
λ_{cap}	Thermal conductivity of caprock, W/(m·K)
λ_{cs}	Thermal conductivity of cement sheath, W/(m·K)
λ_f	Thermal conductivity of the working fluid, W/(m·K)
λ_{HDR}	Thermal conductivity of the hot dry rock, W/(m·K)
λ_{if}	Thermal conductivity of insulation formation, W/(m·K)
λ_s	Thermal conductivity of the impermeable media, W/(m·K)
λ_{top}	Thermal conductivity of the medium at the upper boundary of the model, W/(m·K)
λ_{tran}	Thermal conductivity of the transition formation, W/(m·K)
λ_{TIP}	Thermal conductivity of the thermal insulation pipe, W/(m·K)
ρ_f	Density of the working fluid, kg/m^3
ρ_s	Density of the impermeable media, kg/m^3
Δt	Time step, day
ΔT_{sense}	Outlet temperature variation within the variation range of the sensitivity parameter, ℃
Δx	Discrete radial spacing, m
Δz	Discrete longitudinal spacing, m
δT_{out}	Change in outlet temperature over time, ℃
η_{rmax}	Maximum heat recovery ratio, %
η_s	Heat recovery ratio, %

Acknowledgements
The authors gratefully appreciate the National Nature Science Foundation of China (42220104002).

Author contributions
GS-H: writing original draft, conceptualization, visualization, methodology, validation, formal analysis and project administration. XY-H: project administrator, methodology, conceptualization. HL-M: conceptualization, visualization, methodology, formal analysis. LL: visualization, validation. JY: visualization, validation. WL-Z: visualization, formal analysis. WY-L: visualization, validation. NB-B: visualization, formal analysis. All authors read and approved the final manuscript.

Funding
This work was funded by the National Nature Science Foundation of China (42220104002).

Availability of data and materials
Data associated with this research are confidential and cannot be released. Although it is presented here, they are shown for analysis purposes.

Declarations

Competing interests
The authors declare that they have no known competing financial interests or personal relationships that could have appeared to influence the work reported in this paper.

Received: 6 July 2022 Accepted: 1 February 2023
Published online: 22 February 2023

References

Abdi H. Coefficient of variation. Encycl Res Des. 2010;1:169–71.
Adams BM, Kuehn TH, Bielicki JM, Randolph JB, Saar MO. On the importance of the thermosiphon effect in CPG (CO2 plume geothermal) power systems. Energy. 2014;69:409–18. https://doi.org/10.1016/j.energy.2014.03.032.
Aliyu MD, Chen H-P. Sensitivity analysis of deep geothermal reservoir: effect of reservoir parameters on production temperature. Energy. 2017;129:101–13. https://doi.org/10.1016/j.energy.2017.04.091.
Angrisani G, Diglio G, Sasso M, Calise F, d'Accadia MD. Design of a novel geothermal heating and cooling system: energy and economic analysis. Energy Convers Manage. 2016;108:144–59. https://doi.org/10.1016/j.enconman.2015.11.001.
Anyim K, Gan Q. Fault zone exploitation in geothermal reservoirs: production optimization, permeability evolution and induced seismicity. Adv Geo-Energy Res. 2020. https://doi.org/10.26804/ager.2020.01.01.
Arat H, Arslan O. Exergoeconomic analysis of district heating system boosted by the geothermal heat pump. Energy. 2017;119:1159–70. https://doi.org/10.1016/j.energy.2016.11.073.
Asai P, Panja P, McLennan J, Moore J. Performance evaluation of enhanced geothermal system (EGS): surrogate models, sensitivity study and ranking key parameters. Renew Energy. 2018;122:184–95. https://doi.org/10.1016/j.renene.2018.01.098.
Balbay A, Esen M. Temperature distributions in pavement and bridge slabs heated by using vertical ground-source heat pump systems. Acta Sci Technol. 2013;35(4):677–85. https://doi.org/10.4025/actascitechnol.v35i4.15712.
Bina SM, Jalilinasrabady S, Fujii H. Exergoeconomic analysis and optimization of single and double flash cycles for Sabalan geothermal power plant. Geothermics. 2018;72:74–82. https://doi.org/10.1016/j.geothermics.2017.10.013.
Brown DW, Duchane DV. Scientific progress on the Fenton Hill HDR project since 1983. Geothermics. 1999;28(4–5):591–601. https://doi.org/10.1016/s0375-6505(99)00030-9.
Brown D, DuTeaux R, Kruger P, Swenson D, Yamaguchi T. Fluid circulation and heat extraction from engineered geothermal reservoirs. Geothermics. 1999;28(4–5):553–72. https://doi.org/10.1016/s0375-6505(99)00028-0.
Brown DW. A hot dry rock geothermal energy concept utilizing supercritical CO2 instead of water. Proceedings of the twenty-fifth workshop on geothermal reservoir engineering, Stanford University; 2000: Citeseer.
Bu X, Ma W, Li H. Geothermal energy production utilizing abandoned oil and gas wells. Renewable Energy. 2012;41:80–5. https://doi.org/10.1016/j.renene.2011.10.009.
Bulmez A, Ciofoaia V, Năstase G, Dragomir G, Brezeanu A, Şerban A. An experimental work on the performance of a solar-assisted ground-coupled heat pump using a horizontal ground heat exchanger. Renew Energy. 2022;183:849–65. https://doi.org/10.1016/j.renene.2021.11.064.
Cheng W-L, Li T-T, Nian Y-L, Wang C-L. Studies on geothermal power generation using abandoned oil wells. Energy. 2013;59:248–54. https://doi.org/10.1016/j.energy.2013.07.008.
Cui G, Ren S, Zhang L, Ezekiel J, Enechukwu C, Wang Y, et al. Geothermal exploitation from hot dry rocks via recycling heat transmission fluid in a horizontal well. Energy. 2017;128:366–77. https://doi.org/10.1016/j.energy.2017.04.027.
Davis AP, Michaelides EE. Geothermal power production from abandoned oil wells. Energy. 2009;34(7):866–72. https://doi.org/10.1016/j.energy.2009.03.017.
Esen H, Inalli M, Esen M, Pihtili K. Energy and exergy analysis of a ground-coupled heat pump system with two horizontal ground heat exchangers. Build Environ. 2007a;42(10):3606–15. https://doi.org/10.1016/j.buildenv.2006.10.014.
Esen H, Inalli M, Esen M. Numerical and experimental analysis of a horizontal ground-coupled heat pump system. Build Environ. 2007b;42(3):1126–34. https://doi.org/10.1016/j.buildenv.2005.11.027.
Ewing RE, Lazarov RD, Vassilev TA. Finite difference scheme for parabolic problems on composite grids with refinement in time and space. SIAM J Numer Anal. 1994;31(6):1605–22. https://doi.org/10.1137/0731083.
Fang L. Heat transfer analysis and application of deep borehole heat exchanger in ground source heat pump system. PhD thesis, Shandong Jianzhu University. 2018.
Gharibi S, Mortezazadeh E, Bodi SJHA, Vatani A. Feasibility study of geothermal heat extraction from abandoned oil wells using a U-tube heat exchanger. Energy. 2018;153:554–67. https://doi.org/10.1016/j.energy.2018.04.003.
Go GH, Lee SR, Yoon S, Kim MJ. Optimum design of horizontal ground-coupled heat pump systems using spiral-coil-loop heat exchangers. Appl Energy. 2016;162:330–45. https://doi.org/10.1016/j.apenergy.2015.10.113.
Gong F, Guo T, Sun W, Li Z, Yang B, Chen Y, Qu Z. Evaluation of geothermal energy extraction in Enhanced Geothermal System (EGS) with multiple fracturing horizontal wells (MFHW). Renew Energy. 2020;151:1339–51. https://doi.org/10.1016/j.renene.2019.11.134.

Gonzalez RG, Verhoef A, Vidale PL, Main B, Gan G, Wu Y. Interactions between the physical soil environment and a horizontal ground coupled heat pump, for a domestic site in the UK. Renew Energy. 2012;44:141–53. https://doi.org/10.1016/j.renene.2012.01.080.
Gupta HK, Roy S. Geothermal energy: an alternative resource for the 21st century. Amsterdam: Elsevier; 2006.
Hendron RH. The US hot dry rock project. Los Alamos National Lab.(LANL), Los Alamos, NM (United States); 1987. https://www.osti.gov/biblio/888488.
Huang G, Ma H, Hu X, Cai J, Li J, Luo H, et al. A coupled model of two-phase fluid flow and heat transfer to transient temperature distribution and seepage characteristics for water-flooding production well with multiple pay zones. Energies. 2019;12(10):1854. https://doi.org/10.3390/en12101854.
Kraft T, Deichmann N. High-precision relocation and focal mechanism of the injection-induced seismicity at the Basel EGS. Geothermics. 2014;52:59–73. https://doi.org/10.1016/j.geothermics.2014.05.014.
Kujawa T, Nowak W, Stachel AA. Heat-flow characteristics of one-hole and two-hole systems for winning geothermal heat. Appl Energy. 2003;74(1–2):21–31. https://doi.org/10.1016/S0306-2619(02)00127-7.
Kujawa T, Nowak W, Stachel A. Analysis of the exploitation of existing deep production wells for acquiring geothermal energy. J Eng Phys Thermophys. 2005;78(1):127–35. https://doi.org/10.1007/s10891-005-0038-1.
Kujawa T, Nowak W, Szaflik W, editors. Mathematical model of a geothermal Field exchanger. Institute of Mathematics and its applications conference series; 1998: Oxford University Press.
Kujawa T, Nowak W, Stachel AA, editors. Utilization of existing deep geological wells for acquisitions of geothermal energy. Thermal Sciences 2004 Proceedings of the ASME-ZSIS International Thermal Science Seminar II; 2004: Begel House Inc. https://doi.org/10.1615/ICHMT.2004.IntThermSciSemin.680.
Lazarov R, Mishev ID, Vassilevski PS. Finite volume methods for convection-diffusion problems. SIAM J Numer Anal. 1996;33(1):31–55. https://doi.org/10.1137/0733003.
Lee KS. Effects of regional groundwater flow on the performance of an aquifer thermal energy storage system under continuous operation. Hydrogeol J. 2014;22(1):251–62. https://doi.org/10.1007/s10040-013-1052-6.
Li J, Zhang Y. GIS-supported certainty factor (CF) models for assessment of geothermal potential: a case study of Tengchong County, southwest China. Energy. 2017;140:552–65. https://doi.org/10.1016/j.energy.2017.09.012.
Li H, Jiang X, Xu Z, Bowden S. The effect of supercritical CO_2 on failure mechanisms of hot dry rock. Adv Geo-Energy Res. 2022;6(4):324–33. https://doi.org/10.46690/ager.2022.04.07.
Liu Y, Hou J, Zhao H, Liu X, Xia Z. A method to recover natural gas hydrates with geothermal energy conveyed by CO_2. Energy. 2018;144:265–78. https://doi.org/10.1016/j.energy.2017.12.030.
Lu SM. A global review of enhanced geothermal system (EGS). Renew Sustain Energy Rev. 2018;81:2902–21. https://doi.org/10.1016/j.rser.2017.06.097.
Majer EL, Baria R, Stark M, Oates S, Bommer J, Smith B, et al. Induced seismicity associated with enhanced geothermal systems. Geothermics. 2007;36(3):185–222. https://doi.org/10.1016/j.geothermics.2007.03.003.
McAuliffe RE. Coefficient of variation. Wiley Encyclopedia of Management. 2015:39.
Mokhtari H, Hadiannasab H, Mostafavi M, Ahmadibeni A, Shahriari B. Determination of optimum geothermal Rankine cycle parameters utilizing coaxial heat exchanger. Energy. 2016;102:260–75. https://doi.org/10.1016/j.energy.2016.02.067.
Nian YL, Cheng WL. Insights into geothermal utilization of abandoned oil and gas wells. Renew Sustain Energy Rev. 2018;87:44–60. https://doi.org/10.1016/j.rser.2018.02.004.
None N. An evaluation of enhanced geothermal systems technology. EERE Publication and Product Library, Washington, DC (United States); 2009. http://dx.doi.org/https://doi.org/10.2172/1217838.
Pruess K. Enhanced geothermal systems (EGS) using CO_2 as working fluid—a novel approach for generating renewable energy with simultaneous sequestration of carbon. Geothermics. 2006;35(4):351–67. https://doi.org/10.1016/j.geothermics.2006.08.002.
Sayigh A. Renewable energy—the way forward. Appl Energy. 1999;64(1–4):15–30. https://doi.org/10.1016/j.energy.2014.03.032.
Seyedrahimi-Niaraq M, Bina SM, Itoi R. Numerical and thermodynamic modeling for estimating production capacity of NW Sabalan geothermal field. Iran Geothermics. 2021a;90: 101981. https://doi.org/10.1016/j.geothermics.2020.101981.
Seyedrahimi-Niaraq M, Ardejani FD, Noorollahi Y, Nasrabadi SJ, Hekmatnejad A. An unsaturated three-dimensional model of fluid flow and heat transfer in NW Sabalan geothermal reservoir. Geothermics. 2021b;89: 101966. https://doi.org/10.1016/j.geothermics.2020.101966.
Shi Y, Song X, Li G, Li R, Zhang Y, Wang G, et al. Numerical investigation on heat extraction performance of a downhole heat exchanger geothermal system. Appl Therm Eng. 2018;134:513–26. https://doi.org/10.1016/j.applthermaleng.2018.02.002.
Shi Y, Song X, Li J, Wang G, Zheng R, YuLong F. Numerical investigation on heat extraction performance of a multilateral-well enhanced geothermal system with a discrete fracture network. Fuel. 2019;244:207–26. https://doi.org/10.1016/j.fuel.2019.01.164.
Shi, M. Fully implicit upwind finite difference scheme and iterative method for nonlinear convection-diffusion equations. Master's Thesis, Northeast Normal University. 2021.
Su Y, Sun N. Horizontal drilling technology: present and future. Oil Dril Prod Technol. 1996(06):14–20+96–7. https://doi.org/10.13639/j.odpt.1996.06.003.
Sun F, Yao Y, Li G, Li X. Geothermal energy extraction in CO_2 rich basin using abandoned horizontal wells. Energy. 2018;158:760–73. https://doi.org/10.1016/j.energy.2018.06.084.
Wang X, Liu C. Pressure analysis for horizontal wells in composite reservoirs. Acta Petrolei Sinica. 1997;02:75–80. https://doi.org/10.7623/syxb199702012.
Wang X, Wu N, Su Z, Zend Y. Progress of the enhanced geothermal systems (EGS) development technology. Prog Geophys. 2012a;27(1):355–62.
Wang XX, Wu NY, Su Z, Zeng YC. Progress of the enhanced geothermal systems (EGS) development technology. Prog Geophys. 2012b;27(1):355–62. https://doi.org/10.6038/j.issn.1004-2903.2012.01.041.

Wang CL, Cheng WL, Nian YL, Yang L, Han B-B, Liu M-H. Simulation of heat extraction from CO2-based enhanced geothermal systems considering CO_2 sequestration. Energy. 2018;142:157–67. https://doi.org/10.1016/j.energy.2017.09.139.
Wang Z. Study on heat extraction characteristics of underground coaxial heat exchangers for medium and deep geothermal. Master's Thesis, Hebei University of Engineering. 2019.
Willems CJ, Nick HM, Weltje GJ, Bruhn DF. An evaluation of interferences in heat production from low enthalpy geothermal doublets systems. Energy. 2017;135:500–12. https://doi.org/10.1016/j.energy.2017.06.129.
Wu Z, Gong Y, Ma W, Deng S. Research on geothermal power generation by flash system combined with binary cycle. Acta Energiae Solaris Sinica. 2009;30(3):316–21.
Xu T, Pruess K. Numerical simulation of injectivity effects of mineral scaling and clay swelling in a fractured geothermal reservoir. Lawrence Berkeley National Lab.(LBNL), Berkeley, CA (United States); 2004. https://www.osti.gov/biblio/834641.
Xu, B. Study on heat transfer characteristics of the middle-deep coaxial casing ground heat exchanger. Master's Thesis, Hebei University of Engineering. 2020.
Yuan Y. Theory and application of upwind finite difference method for moving boundary value problem of three-dimensional percolation coupled system. Sci China Math. 2010;40(2):103–26.
Zeng Y, Tang L, Wu N, Cao Y. Analysis of influencing factors of production performance of enhanced geothermal system: a case study at Yangbajing geothermal field. Energy. 2017;127:218–35. https://doi.org/10.1016/j.energy.2017.03.100.
Zhang FZ, Jiang PX, Xu RN. System thermodynamic performance comparison of CO_2-EGS and water-EGS systems. Appl Therm Eng. 2013;61(2):236–44. https://doi.org/10.1016/j.applthermaleng.2013.08.007.
Zhang W, Wang J, Zhang F, Lu W, Cui P, Guan C, Yu M, Fang Z. Heat transfer analysis of U-type deep borehole heat exchangers of geothermal energy. Energy Build. 2021;237: 110794. https://doi.org/10.1016/j.enbuild.2021.110794.

Publisher's Note